



UNIVERSITY OF LEEDS

This is a repository copy of *3-D uncertainty-based topographic change detection with structure-from-motion photogrammetry: precision maps for ground control and directly georeferenced surveys*.

White Rose Research Online URL for this paper:
<http://eprints.whiterose.ac.uk/112711/>

Version: Accepted Version

Article:

James, MR, Robson, S and Smith, MW orcid.org/0000-0003-4361-9527 (2017) 3-D uncertainty-based topographic change detection with structure-from-motion photogrammetry: precision maps for ground control and directly georeferenced surveys. *Earth Surface Processes and Landforms*, 42 (12). pp. 1769-1788. ISSN 0197-9337

<https://doi.org/10.1002/esp.4125>

© 2017, Wiley. This is the peer reviewed version of the following article: "James, M. R., Robson, S., and Smith, M. W. (2017) 3-D uncertainty-based topographic change detection with structure-from-motion photogrammetry: precision maps for ground control and directly georeferenced surveys. *Earth Surf. Process. Landforms*" which has been published in final form at <http://doi.org/10.1002/esp.4125>. This article may be used for non-commercial purposes in accordance with Wiley Terms and Conditions for Self-Archiving.

Reuse

Items deposited in White Rose Research Online are protected by copyright, with all rights reserved unless indicated otherwise. They may be downloaded and/or printed for private study, or other acts as permitted by national copyright laws. The publisher or other rights holders may allow further reproduction and re-use of the full text version. This is indicated by the licence information on the White Rose Research Online record for the item.

Takedown

If you consider content in White Rose Research Online to be in breach of UK law, please notify us by emailing eprints@whiterose.ac.uk including the URL of the record and the reason for the withdrawal request.



eprints@whiterose.ac.uk
<https://eprints.whiterose.ac.uk/>

1 **3-D uncertainty-based topographic change detection with structure-from-**
2 **motion photogrammetry: precision maps for ground control and directly**
3 **georeferenced surveys**

4
5 James, M. R.^a, Robson, S.^b and Smith, M. W.^c

6
7 ^aLancaster Environment Centre, Lancaster University, Lancaster, LA1 4YQ, U.K.

8 (corresponding author: m.james@lancs.ac.uk, +44 (0)1524 593571)

9 ^bDepartment of Civil, Environmental and Geomatic Engineering, University

10 College London, Gower Street, London, WC1E 6BT, U.K.

11 ^cSchool of Geography, University of Leeds, Leeds, LS2 9JT, U.K.

12
13 Short title: *3-D uncertainty-based change detection for SfM surveys*

14
15 **Abstract**

16 Structure-from-motion (SfM) photogrammetry is revolutionising the collection of
17 detailed topographic data, but insight into geomorphological processes is currently
18 restricted by our limited understanding of SfM survey uncertainties. Here, we present
19 an approach that, for the first time, specifically accounts for the spatially variable
20 precision inherent to photo-based surveys, and enables confidence-bounded
21 quantification of 3-D topographic change. The method uses novel 3-D precision
22 maps that describe the 3-D photogrammetric and georeferencing uncertainty, and
23 determines change through an adapted state-of-the-art fully 3-D point-cloud
24 comparison (M3C2; Lague, *et al.*, 2013), which is particularly valuable for complex
25 topography. We introduce this method by: (1) using simulated UAV surveys,

26 processed in photogrammetric software, to illustrate the spatial variability of precision
27 and the relative influences of photogrammetric (e.g. image network geometry, tie
28 point quality) and georeferencing (e.g. control measurement) considerations; (2) we
29 then present a new Monte Carlo procedure for deriving this information using
30 standard SfM software and integrate it into confidence-bounded change detection;
31 before (3) demonstrating geomorphological application in which we use benchmark
32 TLS data for validation and then estimate sediment budgets through differencing
33 annual SfM surveys of an eroding badland. We show how 3-D precision maps
34 enable more probable erosion patterns to be identified than existing analyses, and
35 how a similar overall survey precision could have been achieved with direct survey
36 georeferencing for camera position data with precision half as good as the GCPs'.
37 Where precision is limited by weak georeferencing (e.g. camera positions with multi-
38 metre precision, such as from a consumer UAV), then overall survey precision can
39 scale as $n^{-1/2}$ of the control precision (n = number of images). Our method also
40 provides variance-covariance information for all parameters. Thus, we now open the
41 door for SfM practitioners to use the comprehensive analyses that have underpinned
42 rigorous photogrammetric approaches over the last half-century.

43

44 **Keywords:** precision maps, DEM uncertainty, structure-from-motion,
45 georeferencing, UAV

46 **Introduction**

47 Detailed digital elevation models (DEMs) produced by high resolution
48 topography (HiRT) measurement techniques are accelerating our understanding of
49 geomorphological processes. Increasingly, digital photographs are being used to
50 generate such topographic data (particularly from consumer cameras and unmanned
51 aerial vehicles (UAVs)), supported by processing software based on structure from
52 motion (SfM). Such techniques are being used to, for example, model fluvial
53 processes and drive hydraulic models (Dietrich, 2016; Javernick, *et al.*, 2016;
54 Woodget, *et al.*, 2015), reconstruct the propagation of glacial outburst floods
55 (Westoby, *et al.*, 2015), understand wave run-up and coastal cliff erosion (Casella, *et*
56 *al.*, 2014; James and Robson, 2012), quantify eroded soil and gully volumes
57 (Castillo, *et al.*, 2012; Eltner, *et al.*, 2015; Gomez-Gutierrez, *et al.*, 2014), examine
58 landslide and glacier movement (Lucieer, *et al.*, 2014; Ryan, *et al.*, 2015),
59 characterise ice surface roughness to parameterise surface melt models (Smith, *et*
60 *al.*, 2016) and determine the evolution of active lava flows and domes (James and
61 Robson, 2014b; James and Varley, 2012). The flexibility of SfM-processing enables
62 a wide range of imagery and imaging geometries to be used and is central to the
63 widespread adoption of HiRT techniques. However, this flexibility can result in
64 substantial variations in data quality, both between and, crucially, within surveys
65 (Smith and Vericat, 2015), which is often poorly quantified. Here, we derive and
66 demonstrate a novel approach to enable rigorous and confidence-bounded change
67 detection in complex topography from photo-based surveys, based on precision
68 maps which characterise the 3-D survey quality and its spatial variability. Whilst we
69 focus on airborne surveys, the approach is of equal value for terrestrially-acquired
70 data.

71 *DEM uncertainty*

72 Understanding survey uncertainties is critical for appropriate error propagation
73 into downstream topographic analyses, and the importance of DEM uncertainty
74 when deriving geomorphological parameters and associated process models has
75 been widely demonstrated (e.g. Lallias-Tacon, *et al.*, 2014; Milan, *et al.*, 2011;
76 Wheaton, *et al.*, 2010). When determining topographic change (e.g. for estimating
77 sediment budgets), vertical uncertainty can be considered for conventional DEMs of
78 difference (DoDs) to enable the significance of changes to be estimated (Brasington,
79 *et al.*, 2003; Lane, *et al.*, 2003). Changes smaller than a specified 'level of detection'
80 (LoD) can then be disregarded where, for two DEMs with vertical standard deviations
81 of error, σ_{z1} and σ_{z2} ,

$$82 \text{LoD} = t(\sigma_{z1}^2 + \sigma_{z2}^2)^{1/2} \quad 1),$$

83 and t is an appropriate value for the required confidence level. LoD values are
84 typically calculated to represent a 95% confidence level (i.e. LoD_{95%}), for which,
85 under the t distribution, $t = 1.96$.

86 Single LoD values for use across entire DoDs can be estimated from relatively
87 standard error assessments such as the root mean square error (RMSE) on
88 independently surveyed check points for the constituent DEMs (e.g. Milan, *et al.*,
89 2007). Although such RMSE values can provide valuable insight into overall survey
90 performance, they do not expose the spatial variability that can be highly relevant for
91 detailed DEM analyses (Chu, *et al.*, 2014; Gonga-Saholiariliva, *et al.*, 2011; Oksanen
92 and Sarjakoski, 2006; Weng, 2002) and their use can result in issues such as
93 significant volumes from small elevation changes over large areas being neglected
94 (e.g. overbank deposition, Brasington, *et al.*, 2003). More challengingly, spatially
95 variable LoD values can be determined, either manually, via classification from other
96 information, or through using underlying data to estimate parameters such as sub-

97 grid roughness (Brasington, *et al.*, 2003; Lane, *et al.*, 2003; Wheaton, *et al.*, 2010).
98 However, by disregarding horizontal error through conventional use of (2.5-D) DEMs,
99 uncertainty estimates for topographic change detection (which include precision and
100 accuracy components) can lose validity in regions of steep topography (Lague, *et al.*,
101 2013).

102 *3-D analysis and photo-based surveys*

103 Consequently, and to take full advantage of large and fully 3-D datasets such as
104 from terrestrial laser scanners (TLSs), multiple methods for directly comparing point
105 clouds have been derived (see Lague, *et al.* (2013) for a useful summary). One
106 approach, Multiscale Model to Model Cloud Comparison (M3C2; Lague, *et al.*, 2013)
107 is of particular use in geomorphology because it incorporates a confidence interval
108 and thus provides 3-D analysis of topographic change constrained by spatially
109 variable $LoD_{95\%}$ values, and is applicable in any type of terrain. Within the M3C2
110 algorithm, measurement precision is estimated from local surface roughness, which
111 is highly appropriate for the TLS data for which it was primarily designed. However,
112 the smoothing or filtering commonly incorporated into image matching algorithms
113 (e.g. Furukawa and Ponce, 2007; Hirschmuller, 2008) can strongly mute the
114 representation of small-scale roughness in photo-derived point clouds. Furthermore,
115 the complex photogrammetric and georeferencing processes result in point
116 coordinate precision being a function of survey characteristics such as image
117 network geometry and the quality, quantity and distribution of control, leading to point
118 position errors that are spatially variable but locally highly correlated (due to
119 neighbouring points generally being derived from the same images and thus subject
120 to similar error). Thus, purely roughness-based precision estimates are unlikely to be
121 representative of uncertainty in photogrammetric point clouds.

122 As for all topographic measurement techniques, the georeferencing process is
123 central to achieving data with suitable repeatability (i.e. good spatial precision) for
124 detecting change and, for photo-based surveys, georeferencing is usually carried out
125 by measuring ground control points (GCPs). However, the deployment and precise
126 ground survey of GCP arrays can require considerable effort, as well as the
127 availability of relatively expensive survey equipment (e.g. dGPS or total station), and
128 this can offset the otherwise cost-effective combination of UAV and SfM-MVS
129 processing. An alternative is 'direct georeferencing', in which control is provided
130 through measurements of camera orientations only (e.g. Cramer, *et al.*, 2000;
131 Förstner, *et al.*, 2013). By not requiring ground-based measurements, the direct
132 approach has a critical advantage for aerial survey over hazardous terrain, and has
133 been shown capable of measurement precisions of order 0.1 m for piloted SfM-
134 based surveys with survey-grade GPS synchronised with image capture (Nolan and
135 DesLauriers, 2016; Nolan, *et al.*, 2015). However, for most current consumer UAVs,
136 precise directly georeferenced work is prevented by their use of low-quality, multi-
137 metre precision, on board GPS (Carbonneau and Dietrich, 2016) but survey-grade
138 GPS is being increasingly installed (e.g. Bláha, *et al.*, 2011; Chiang, *et al.*, 2012;
139 Eling, *et al.*, 2015; Gabrlik, 2015; Hugenholtz, *et al.*, 2016; Mian, *et al.*, 2015; Rehak,
140 *et al.*, 2013; Turner, *et al.*, 2014) and such systems are likely to develop into
141 widespread, invaluable tools for geomorphological research. Consequently,
142 understanding the differences in survey performance between using GCPs or direct
143 georeferencing will be integral to optimising future survey strategies aimed at
144 quantifying topography and topographic change.

145 Here, we have the overall aims of enabling uncertainty-bounded analysis of
146 topographic change using SfM and exploring the implications of different
147 georeferencing styles. Our approach is based on deriving maps of 3-D precision

148 from the precision estimates that are integral to rigorous photogrammetric
149 processing, and which capture the variation of both photogrammetric and
150 georeferencing uncertainties across the full extent of surveys. Within the paper, we
151 initially summarise how precision estimates are derived during photogrammetric
152 processing and then (1), we introduce the insight that precision maps provide into
153 spatial variability and sensitivity to survey and georeferencing parameters, using
154 simulated UAV surveys processed with rigorous close-range photogrammetric
155 software. Unfortunately, the current range of SfM-based software commonly used to
156 process most geomorphological surveys does not yet offer detailed precision
157 information. Thus (2), we implement a novel Monte Carlo approach that enables
158 precision maps to be produced when using SfM-based software, and we integrate
159 the resulting precision estimates with the M3C2 algorithm to enable confidence-
160 bounded 3-D change measurement for photo-based surveys. Finally (3), we
161 demonstrate our method on an eroding badlands catchment where erosion
162 assessments over $\sim 4,700 \text{ m}^2$ require sub-decimetre level precision (Smith and
163 Vericat, 2015).

164 **Photogrammetric precision estimates**

165 Precision estimates are an integral component of rigorous photogrammetric
166 processing and result from the optimisation procedures used when deriving 3-D
167 information from photographs (Cooper and Robson, 1996; Förstner and Wrobel,
168 2013). Here, and throughout, we use ‘precision’ to refer to the expected one
169 standard deviation of an estimated or measured value. Image processing comprises
170 the automatic identification of ‘tie point’ features (often tens of thousands) in the
171 images, matching them across multiple images, and making initial estimates of their
172 3-D point coordinates from the two-dimensional image observations. In

173 geomorphological surveys, the tie points within this image network usually represent
174 distinct features on the ground (such as, depending on image scale, grains,
175 boulders, the edges of rills) and thus their positions map the topographic surface
176 (Figure 1a). Subsequent photogrammetric processing is based on ‘bundle
177 adjustment’, a least-squares global optimisation which minimises the total residual
178 error on image observations by simultaneously adjusting camera parameters and
179 orientations, and the 3-D point positions (Granshaw, 1980). Just as when applying a
180 linear model to multiple measurements of two variables, the observational
181 redundancy within the bundle adjustment (due to the large number of tie points) and
182 the use of a least-squares approach enables precision estimates to be derived for all
183 adjusted model parameters. These parameters include camera models and the 3-D
184 point positions and, by also considering variances and covariances, correlations
185 between camera parameters can be identified, and each tie point can be
186 accompanied by a 3-D measurement precision ellipsoid (Figure 1a). The point
187 precision estimates can be used to define the repeatability of measurements made
188 within the results (e.g. relative distances between points), given the error associated
189 with the input measurements (i.e. the tie point image observations). Our precision
190 maps are based on the 3-D precision estimates made for the tie point coordinates,
191 and are thus most effective for dense distributions of tie points.

192 Control measurements are included within an adjustment to introduce an
193 external coordinate system in which the precision estimates are reported and the
194 survey is georeferenced (Figure 1b). Typically, to ensure geometric coverage over
195 the entire survey area, more control measurements are used than the minimum
196 required to uniquely define the coordinate datum and, thus, the relative shape of the
197 survey can also be influenced. Each control measurement (e.g. a dGPS ground
198 survey measurement of a control point position, or a camera position) is

199 characterised by a defined measurement precision that is included within the
200 adjustment calculations; consequently, if control is only given to poor precision, then
201 this propagates through to, and can dominate, the derived 3-D topographic point
202 coordinate precision values (Figure 1c). In this case, although the overall precision of
203 point locations within the external coordinate system is degraded by the poor control
204 measurement precision, relative distances between points within the survey may
205 remain precise (i.e. with the 'internal' precision of the survey controlled by the quality
206 of the tie points, Figure 1a).

207 Another way of considering this is that the relative shape of the topographic
208 surface derived internally within the photogrammetric network may be good, but its
209 overall georeferencing to an external coordinate system (as defined by a best-fit
210 Helmert transform, comprising scale, rotation and translation components (Förstner,
211 *et al.*, 2013)) is weakly constrained. Thus, the final surface model precision can be
212 separated into components of the external coordinate system georeference, and the
213 shape of the model (e.g. Förstner, *et al.* (2013); a concept also used recently for
214 DEM error (Carbonneau and Dietrich, 2016)). Through separating the georeference
215 and the surface shape components of the precision estimates, insight can be gained
216 into the relative contributions of control measurements and tie points – i.e. how
217 important the control measurements are in influencing the shape of a survey as well
218 as for overall georeferencing.

219 Within a photogrammetric workflow, precision estimation precedes, and is
220 independent from, the dense image matching from which DEMs are ultimately
221 derived. However, the dense matching process does not optimise any aspects of the
222 image network and, therefore, does not affect the underlying precision estimates.
223 Additional error can be introduced by the dense matching itself, but work on early
224 stereo-matching algorithms (Lane, *et al.*, 2000) found this to be less important for

225 resulting DEMs than issues such as the presence of vegetation and data resolution.
226 With error from modern multi-image dense matching algorithms likely to be less than
227 from early stereo-matchers, in this work, we consider that tie point precision can be
228 used to represent the main measurement contribution to surface model precision.

229 Thus, in our approach, we ascribe precision values to the dense cloud points
230 based on the precision of their underlying sparse tie points. Note that, because
231 precision estimates are derived from the least-squares minimisation of image
232 residuals, some systematic errors inherent in photogrammetric processing (such as
233 doming deformation of the surface), which are not detectable in image residuals, are
234 not included in the precision estimates. Such errors represent internal accuracy
235 problems that can be identified by using check points (Chandler, 1999), and have to
236 be mitigated by the use of suitably precise and well-distributed control, an accurate
237 camera model or appropriately strong imaging geometries (James and Robson,
238 2014a; Wackrow and Chandler, 2011). Thus, care needs to be taken to avoid
239 interpreting precision maps as a guarantee of accuracy, which can only be validated
240 through independent check points.

241 **Methodology and case study field site**

242 *Precision maps for survey design: simulated UAV surveys*

243 To demonstrate how precision can vary spatially and with survey characteristics,
244 we first generated precision maps using rigorous photogrammetry software, for
245 simulated UAV surveys with different georeferencing conditions and imaging
246 geometries. The simulated surveys were constructed by initially defining camera
247 models and positions over a virtual surface represented by a grid of 3-D tie points
248 and GCPs. Image observations, including pseudo-random measurement noise to
249 represent image residuals, were then generated for the tie points and GCPs, to

250 complete the image network. Survey flight plans (based on those used in James and
251 Robson (2014a)) were generated with two mutually inclined sets of parallel flight
252 lines, which were augmented for some scenarios by twin gently banked turns in
253 order to include convergent imagery, and hence add strength, to the image network
254 (Figure 2, Table 1). The image networks were then processed by self-calibrating
255 bundle adjustment using the close-range photogrammetry software 'Vision
256 Measurement System' (VMS; <http://www.geomsoft.com>) which provides point
257 precision as a standard output. The simulations were carried out for eight scenarios
258 which covered the combinations of 'weak' or 'strong' control, for both GCPs or direct
259 georeferencing using camera positions, and 'weak' (parallel-only) or 'strong'
260 (augmented with oblique images taken with the same camera, from gently banked
261 turns) image network geometries (Table 1). For the GCP-based simulations, the
262 difference between 'weak' and 'strong' control scenarios was emphasised by also
263 varying the image measurement precision of the tie points and GCPs (Table 1).

264 As well as measurement precision, the results enabled the actual surface error
265 realised in each simulation to be assessed through direct comparison of the
266 processed point positions with their known initial coordinates. Error in the overall
267 georeferencing of surveys was determined by deriving the Helmert transform (the
268 seven-parameter transformation for translation, rotation and scale) that best-fit the
269 processed points to their initial positions. Applying the transform then allowed the
270 residual surface shape error to be given by the remaining discrepancies with the
271 initial coordinates (e.g. Carbonneau and Dietrich, 2016). Note that, in each instance,
272 the errors calculated reflect the particular random offsets applied to the control and
273 tie point measurements for that particular simulation. The errors realised thus
274 represent a specific sampling from the distributions of likely error characterised by
275 the precision values. Consequently, if a simulation was repeatedly processed with

276 different random offsets each time, the distributions of error produced would reflect
277 the precision estimates. Thus, when using SfM software that does not provide
278 detailed precision information (but enables rapid and repeated bundle adjustment),
279 precision estimates can be derived through such a Monte Carlo approach.

280 *Implementing precision maps with SfM surveys*

281 PhotoScan is currently the most commonly used SfM-based software for
282 geomorphological surveys (Eltner, *et al.*, 2016) and supports automated analyses
283 through Python scripts. In order to derive precision maps when using PhotoScan Pro
284 (v. 1.2.3) we implemented a Monte Carlo-based approach (Figure 3, and see
285 electronic supporting information for the Python script and instructions), with post-
286 processing tools integrated into sfm_georef software (tinyurl.com/sfmgeoref; James
287 and Robson, 2012). In summary, the method is founded on repeated bundle
288 adjustments, in which pseudo-random error offsets are used to simulate observation
289 measurement precision within the adjustment. Precision estimates for each
290 optimised model parameter (e.g. each point coordinate or camera parameter value)
291 are then derived by characterising the variance for each particular parameter in the
292 outputs from a suitably large number of adjustments.

293 To start the analysis, images are processed as normal in PhotoScan: image
294 alignment derives camera models, positions and orientations, and a sparse point
295 cloud of 3-D tie points. During the alignment process, georeferencing can be
296 achieved by either including ground control points or camera orientation data as
297 control measurements, with (in version 1.2.3 of PhotoScan) all points or cameras
298 accompanied by individual X, Y and Z components of measurement precision. The
299 photogrammetric network is refined by identifying and removing outlier points, and
300 ensuring that image observations of tie and control point measurements are

301 appropriately weighted (i.e. appropriate values for the ‘tie point accuracy’ and
302 ‘marker accuracy’ settings (James, *et al.*, 2017)). The resulting processed image
303 network represents the geometry from which the dense image matching would be
304 subsequently carried out to derive the DEM (a step that is not required within the
305 Monte Carlo iterations, Figure 3).

306 The Monte Carlo analysis is underpinned by making a simulation copy of the
307 image network which is internally error-free and, from which, each Monte Carlo
308 iteration is then constructed by adding appropriate random error. The error-free
309 network is derived by replacing all control measurements (e.g. surveyed GCP
310 coordinates, or GPS-based camera positions and orientations if using direct
311 georeferencing) with their network-estimated values, and by replacing all image
312 observations with equivalents of zero-magnitude image residual by projecting the 3-
313 D points into the cameras. For each iteration of the analysis, this error-free
314 simulation copy is retrieved and offsets (error) are added to the observations and
315 control measurements. The offsets appropriately represent the measurement
316 precision by being derived from pseudo-random normal distributions with standard
317 deviations given by the corresponding survey measurement precision or the RMS of
318 the original image residuals. A bundle adjustment is carried out and the results
319 exported to file before the next iteration is initiated.

320 The number of iterations to use can be determined by sequentially calculating
321 the variance of the derived point coordinates, and carrying out sufficient iterations for
322 variance estimates to stabilise. Finally, the results from all iterations are compiled to
323 give distributions of determined values for all estimated parameters (e.g. coordinate
324 values for each sparse point, camera model parameters and camera orientation
325 parameters). To construct 3-D precision maps, point coordinate standard deviations
326 (in X , Y and Z) are calculated for each point and interpolated onto a grid, resulting in

327 three raster maps, representing the spatially variable precision in X , Y and Z
328 directions. The influence of outliers (e.g. individual points that may be very poorly
329 matched) is minimised by using a moving median filter for the interpolation, which
330 determines the local median value over a defined radial distance. This is a
331 reasonable first-order approach but certainly not the only possibility, and we leave
332 exploration of alternatives to further work.

333 The Monte Carlo iterations not only enable precision values to be calculated but
334 also the associated covariance. Thus, full point coordinate error ellipsoids can be
335 derived for tie points, and correlation between camera parameters assessed
336 (facilitating valuable checks for over-parameterisation of camera models).
337 Furthermore, by considering the results of each iteration together as an entire
338 surface model, the survey's overall georeferencing precision can be estimated – i.e.
339 how precisely the surface is georeferenced in terms of its scale, translation and
340 rotation. Interpretation of scale and translational precision is relatively
341 straightforward, but rotational transformations are conventionally described by three
342 angles that represent rotations applied sequentially around the X , Y and Z axes as
343 the coordinate system is transformed (e.g. Förstner, *et al.*, 2013). However, their
344 sequential application makes their values (Euler angles) difficult to interpret in field-
345 geomorphological terms such as the resulting uncertainty in topographic slope. Thus,
346 we calculate rotational precision directly in terms of the resulting slope uncertainty
347 from the fixed X and Y axes of the geographic coordinate system (i.e. to give the
348 precision of ground slope measurements in north-south and east-west directions),
349 and a rotation around the Z axis. Finally, the precision estimates enable scale-
350 independent estimates of overall survey quality to be calculated which, by reflecting
351 conventional photogrammetric metrics, strongly facilitate inter-survey comparisons.
352 We provide three such dimensionless relative precision ratios (for alternative

353 suggestions see Eltner, *et al.* (2016) and Mosbrucker, *et al.* (2017)); firstly, mean
354 point precision against the largest dimension in the survey (i.e. the distance between
355 the furthest points), secondly, mean point precision against the mean viewing
356 distance (e.g. James and Robson, 2012) and, lastly, mean point precision (as either
357 the horizontal or vertical component) expressed in pixels.

358 *Change detection with 3-D precision maps*

359 With the spatially variable measurement precision given by maps of 3-D
360 precision, confidence intervals for the detection of change between surveys can be
361 determined. To maintain rigour when analysing complex topography, planimetric as
362 well as vertical precision must be considered, and thus we compare dense 3-D point
363 clouds directly, rather than using DEM products. Building on the current state-of-the-
364 art, we base our approach on the full 3-D comparison of point cloud data
365 implemented in the M3C2 algorithm (Lague, *et al.*, 2013). A detailed explanation of
366 M3C2 is given by Lague, *et al.* (2013), but we summarise the method here in order
367 to detail our precision map variant, M3C2-PM.

368 In M3C2, a local mean cloud-to-cloud distance is calculated for each selected
369 point in the reference cloud. For speed, these ‘core points’ can be a subset of the
370 original cloud. For each core point, i , the direction of the local surface normal, \mathbf{N} , is
371 determined by fitting a plane to all its neighbours within a distance $D/2$ (Step 1,
372 Figure 4). The position of the local surfaces in each point cloud is then calculated as
373 the mean position of the cloud points that lie within a cylinder of diameter, d (Step 2,
374 Figure 4), oriented along the normal direction, \mathbf{N} , giving two mean positions i_1 and i_2 ,
375 separated by a distance $L_{M3C2}(i, d, D)$. For each cloud, the M3C2 algorithm uses the
376 positional variability along \mathbf{N} within these points (i.e. the local roughness in the
377 normal direction) as a measure of uncertainty in their mean position, enabling a

378 confidence interval (LoD) to be determined for the distance measurement. However,
379 this assumes that the error in each point coordinate measurement is uncorrelated to
380 that in nearby points and this will not be the case for photogrammetric point clouds,
381 where error in adjacent point positions will be highly correlated due to the bundle
382 adjustment process.

383 Thus, we adapt the M3C2 approach for use with photogrammetric point clouds
384 by using M3C2 to determine local normal distances as usual, then incorporating 3-D
385 precision estimates from associated precision maps (Step 3, Figure 4). Precision
386 values (in X , Y and Z) are ascertained directly from the maps for the $i_1 - i_2$ point
387 pairs, representing one-sigma axially-aligned error ellipsoids around each point
388 (Figure 4). Based on established error analysis (Lane, *et al.*, 2003), and equivalent to
389 Equation 1 in Lague, *et al.* (2013), $LoD_{95\%}$ can then be estimated by combining the
390 precision components in the direction of the local surface normal, σ_{N1} and σ_{N2} ,

$$391 \quad LoD_{95\%}(d) = \pm 1 \cdot 96(\sqrt{\sigma_{N1}^2 + \sigma_{N2}^2} + reg) \quad 2),$$

392 where reg is the relative overall registration error between the surveys, assumed
393 isotropic and spatially uniform (Lague, *et al.*, 2013). Note that Lague, *et al.* (2013)
394 took a conservative approach by adding reg directly (as a potential systematic bias),
395 which we retain here. Nevertheless, with the photogrammetric basis of σ_{N1} and σ_{N2}
396 including georeferencing considerations, reg would be zero if both surveys were
397 defined from the same datum. However, if there was uncertainty in the relative
398 datum measurement between the different surveys, a non-zero value could be used.
399 The output from M3C2-PM thus represents 3-D change between point clouds along
400 local normal directions, along with an assessment of whether that change exceeds
401 the local $LoD_{95\%}$ values, derived from the 3-D spatially variable photogrammetric and
402 georeferencing precision.

403 *Case study: Badlands site and data collection*

404 To demonstrate precision maps and M3C2-PM for determining surface change
405 in complex topography, we use a badlands case study from the River Cinca, Central
406 Pyrenees, Spain (Smith and Vericat, 2015). Oblique images were captured of a
407 ~4,700 m² catchment, during two surveys carried out from a piloted gyrocopter flown
408 at ~50 m above ground level, in 2014 and 2015 (Table 2, Figure 5) and processed
409 using GCPs for control (e.g. Figure 5b inset).

410 In 2014, GCP positions were measured by GNSS (a Leica Viva GS15 in RTK
411 mode) to give absolute positions and associated precisions (ranging between ± 7 mm
412 to ± 29 mm in the horizontal, and ± 14 m to ± 41 m in the vertical) which were
413 converted into ED50 UTM (Zone 31 N) coordinates. In 2015, GCP positions were
414 measured with a Leica TPS1200 total station, giving coordinate precision estimates
415 relative to the instrument position. Thus, when converting these into UTM, the
416 uncertainty in the absolute position of the instrument had to be accounted for: the
417 total station position was derived by resection to a primary control network
418 comprising four permanent targets, giving an RMSE of 9 mm (although note that
419 such few targets make reliable RMSE estimation difficult due to comprising only one
420 redundant point). With the primary control network having a mean absolute 3-D
421 quality of 6 mm (see Smith and Vericat (2015) for details), we use an overall value of
422 11 mm for the absolute precision of the total station position in UTM coordinates.

423 In 2014, benchmark TLS data were acquired for comparison (Smith and Vericat,
424 2015) using a Leica C10 with a maximum measurement range of 300 m and
425 manufacturer-stated precisions of 6 mm for position, 4 mm for distance, and 60 μ rad
426 for angle. To minimise gaps caused by occlusion, data from twelve different stations
427 were combined using target-based registration (with 2 mm mean error), based on a
428 floating network of tripod-mounted Leica targets. The target coordinates were

429 measured with the total station which, in turn was registered to the primary control
430 network as in 2015. Thus, UTM precision estimates for the TLS survey were not
431 straightforward, and we use 11 mm for uncertainty in the datum (as for the total
432 station) and a conservative 10 mm for within-survey precision, to cover all instrument
433 measurement and relative scan registration components.

434 *Data processing and analysis*

435 Images were processed in PhotoScan (v.1.2.3). Image observations of the GCPs
436 were collected using a semi-automated oriented patch cross-correlation approach
437 (James, *et al.*, 2017) and network quality checks during initial processing (James, *et*
438 *al.*, 2017) suggested that three GCPs needed to be rejected from the 2014 network
439 as outliers. For both surveys, initial tests for camera model over-parameterisation
440 were carried out based on GCP analysis (James, *et al.*, 2017), and suggested that
441 the optimal camera model comprised focal length, principal point and three radial
442 distortion components (denoted as Model A). To ensure appropriately balanced
443 optimisation within the surveys, the 'marker accuracy' and 'tie point accuracy'
444 processing settings were given the values of the RMS image residual magnitudes on
445 GCPs and tie points respectively (James, *et al.*, 2017). Other PhotoScan processing
446 settings used were: photos aligned with accuracy 'high', pair preselection 'generic', a
447 tie point limit set to 5000 (to help give a dense distribution of tie points for precision
448 analysis), and the coordinate system set to ED50 UTM (Zone 31 N). The Monte
449 Carlo processing comprised 4,000 iterations for each survey (taking ~3-5 hrs per
450 survey on a desktop PC), and the resulting point precision estimates were
451 interpolated over a 1100 × 700 m, 1-m-resolution grid to cover the catchment of
452 interest. Following the precision analysis, dense cloud generation was carried out at
453 'high' quality, with 'aggressive' depth filtering to minimise surface noise.

454 The 2014 SfM survey data were used initially to validate the Monte Carlo
455 approach by comparing the resulting precision estimates with values generated
456 directly by reprocessing the PhotoScan survey in VMS. The survey was also
457 processed using a more complex camera model (Model B, that additionally included
458 two tangential distortion parameters) to verify the choice of camera model and to
459 check for over-parameterisation through assessing the camera parameter
460 correlations and precision information delivered by the Monte Carlo analysis.

461 The SfM survey was then compared to the benchmark TLS survey over the
462 extent of the TLS data, and with areas of denser vegetation cover removed. As an
463 initial assessment of the M3C2-PM approach, four comparisons were carried out: a
464 straightforward DoD, a DoD using a survey-wide $LoD_{95\%}$ and then 3-D cloud-to-cloud
465 comparisons using M3C2 and M3C2-PM. For the DoD comparisons, 0.1-m-
466 resolution DEMs were derived from the dense point clouds using average elevation
467 values in CloudCompare v.2.7.0 (cloudcompare.org). The survey-wide $LoD_{95\%}$ was
468 introduced by conventionally estimating the overall vertical measurement precision of
469 the surveys as 14.9 mm for TLS (the datum uncertainty and within-survey precision
470 added in quadrature) and 36.8 mm for the SfM (based on the Z-RMSE on control
471 points, Table 2), giving $LoD_{95\%} = 78$ mm (Equation 1). To consider 3-D differences,
472 the native M3C2 analysis was run on the underlying point clouds in CloudCompare.
473 Throughout this work, D and d (Figure 4) values of 0.3 m were used to provide areas
474 sufficiently large for good calculation of surface normal but not too large to be
475 adversely affected at slope-scale (the roughness scales of the badland topography
476 can be considered from Figure 5). A reg value of 80 mm was used, based on
477 combining the 3-D RMSE on the SfM control points (79 mm) and the TLS instrument
478 position precision (11 mm), in quadrature. When using M3C2-PM, the
479 photogrammetric and georeferencing precision of the SfM survey was integral within

480 the precision maps, so *reg* only represented the uncertainty in the TLS instrument
481 position (11 mm). The TLS data did not have associated precision maps, so a
482 constant value of 10 mm was used to represent their precision within the survey.

483 The potential for future SfM surveys to be directly georeferenced was
484 investigated by removing the GCPs from the survey processing and using the
485 estimated camera positions as control measurements. Survey precision was then
486 evaluated by carrying out bundle adjustments in VMS with different precision values
487 assigned to the camera position values. Equivalent analyses were also carried out in
488 PhotoScan using the Monte Carlo approach, by applying offsets from pseudo-
489 random distributions (of appropriate standard deviations) to the camera position
490 control data for each Monte Carlo iteration. The results were compared with those
491 from GCP-based georeferencing, with the influence of measurement precision also
492 assessed by varying the precision assigned to the GCPs.

493 Finally, sediment budgets between 2014 and 2015 were derived from the SfM
494 surveys using the same four analyses as the SfM-TLS comparison. A single survey-
495 wide $LoD_{95\%}$ of 80 mm was determined by adding in quadrature the vertical RMS
496 discrepancies on GCPs (on either check or control points, whichever was the
497 greater), and the 11 mm uncertainty in total station instrument position for the 2015
498 survey. For M3C2 processing, using the 3-D RMS discrepancies on GCPs (79 mm
499 for 2014, and 27 mm for 2015, including the total station instrument position
500 precision) as estimates of georeferencing precision resulted in $reg = 83$ mm. Finally,
501 for our M3C2-PM approach, with point precision estimates explicitly including survey
502 georeferencing, *reg* comprised only the total station instrument position precision for
503 the 2015 survey (11 mm).

504 **Results**

505 *Simulated surveys: precision maps and spatial variation*

506 For a simulated UAV survey with weak image network geometry, but strongly
507 georeferenced using GCPs measured to a precision representative of dGPS
508 measurement (Table 1), 3-D point coordinate precisions showed correlations with
509 changes in image overlap (Figure 6a), indicating that precision was being limited by
510 photogrammetric considerations (i.e. the image network geometry, Figure 1b). Error
511 analysis demonstrated the network geometry weakness by identifying systematic
512 doming as surface shape error, which was present despite the use of ground control
513 in the bundle adjustment (Figure 6a). Strengthening the network geometry by
514 including oblique imagery mitigated the doming (James and Robson, 2014a) and
515 generally improved precision through increasing image overlap (Figure 6b). In this
516 case, the well-distributed and precise GCPs provided a strong overall georeferencing
517 of the survey; error in horizontal position was <3 mm and ground slope error
518 (reflecting systematically varying height error) was $<0.005^\circ$ (Figure 6b), representing
519 height errors of <6 mm at the GCPs furthest from the survey centre.

520 If GCPs were only surveyed to relatively poor precision (e.g. 50 mm in X and Y,
521 and 100 mm in Z, Figure 6c) then the weak control would limit overall survey
522 precision (i.e. just as illustrated in the schematic Figure 1c), even if high-quality tie
523 points and strong network geometry mean that the overall surface shape showed
524 little error (Figure 6d). In this case, the strong photogrammetry would provide high
525 precision internal measurements, such as relative line lengths, but the surface was
526 weakly georeferenced within the external coordinate system (e.g. with systematic
527 error in horizontal position of up to 14 mm and slope error of 0.04° shown in Figure
528 6d, which could be critical when estimating changes of sediment distribution in areas
529 of steep terrain, or flow directions in flat terrain). The symmetric radial degradation of

530 precision away from the centroid of GCP control (Figure 6c, d) reflects this
531 uncertainty in overall georeferencing, and is a combination of scale, translational and
532 rotational uncertainty about the centroid of the control measurements (Figure 1c),
533 which is where the datum is defined during the bundle adjustment.

534 Similar relationships were demonstrated for surveys directly georeferenced using
535 knowledge of camera positions – i.e. without the use of GCPs as control points. If
536 on-board dGPS could provide relatively precise camera position data (e.g. 20 mm in
537 the horizontal and 40 mm in the vertical, and carefully synchronised with image
538 acquisition), then survey precision and overall georeferencing error achieved levels
539 equivalent to those given when using the GCPs (Figure 7a, b), although note that
540 this is strongly dependent on the number and spatial distribution of images.
541 However, currently, UAV camera positions are not generally known to such precision
542 (e.g. the GPS on a consumer UAV may provide position at a precision closer to ~2 m
543 in the horizontal and ~4 m in the vertical (Chiang, *et al.*, 2012), in which case 3-D
544 point precision is strongly limited (Figure 7c, d), with weak network geometries
545 developing systematic error in surface shape (Figure 7c). Overall georeferencing
546 errors were represented by horizontal translations and slopes of up to ~0.5 m and
547 0.5° respectively.

548 Thus, precision maps enable valuable insight into predicted survey performance,
549 and therefore represent a useful survey planning tool that highlights the relative
550 influence of photogrammetric (e.g. tie points, imaging geometry) and georeferencing
551 (e.g. control points) aspects in overall survey quality.

552 *Badlands surveys: Precision maps and TLS comparison*

553 For the 2014 SfM badlands survey, the Monte Carlo results showed that 4,000
554 iterations were sufficient to ensure that uncertainty in the point coordinate precision

555 estimates was of order 1 mm (Figure 8a). The coordinate precision values for all tie
556 points were up to ~0.5 m, and demonstrated strong correspondence with the
557 precision estimates made by rigorous bundle adjustment in VMS (Figure 8b),
558 validating the SfM-Monte Carlo approach. The large values were generally located at
559 the survey extents (i.e. similar to the simulations in Figure 6), and far from the
560 catchment of interest and region of GCP deployment (Figure 5d). Over the region
561 immediately surrounding the catchment (i.e. Figure 5e), mean point precisions were
562 ~23 and 26 mm in the horizontal and vertical respectively, with overall survey
563 georeferencing determined to precisions of <6 mm in translation and <0.02° in
564 topographic slope (Table 3) – note that such slope uncertainty represents a vertical
565 precision of 16 mm at a distance of 50 m from the centroid of control.

566 Precision estimates for the camera parameters showed that all parameter values
567 were well resolved (i.e. their magnitudes were much greater than their precisions,
568 Table 3). Assessing correlations between parameters to give insight into any self-
569 calibration problems indicated that, with one exception, parameter correlations were
570 in line with expectations of a good network, with generally small magnitudes,
571 excluding between the radial distortion terms (Table 4, Camera model A). The block
572 of high-magnitude correlations between radial terms is usual, and results directly
573 from the polynomial representation of the radial distortion model (Clarke and Fryer,
574 1998; Tang and Fritsch, 2013). The exception was the abnormally high correlation
575 between the principal point offset in y and the principal distance. This suggests a
576 slight network weakness that is usually associated with the absence of large camera
577 rotations (i.e. a lack of images taken from similar positions, with ‘portrait’ as well as
578 ‘landscape’ orientations, which is often omitted in UAV surveys); a detailed analysis
579 is out of scope of this paper but see Luhmann, *et al.* (2006) for further information on
580 camera calibration. When the more complex camera model was used (Table 4,

581 Model B), the correlation analysis clearly demonstrated that the increased number of
582 parameters was not appropriate; when tangential distortion terms were included,
583 they showed high correlations with principal point and principal distance terms and
584 no improvements to tie point RMSE or fit to check points were observed. Thus,
585 Model B was deemed over-parameterised and Model A was retained, supporting the
586 initial GCP-based assessment.

587 The relative precision estimates for the full survey indicated that, in comparison
588 with previously published SfM work, it was towards the high-quality end, with a ratio
589 of mean precision against mean observation distance of 1:4,100 (Table 3). The
590 geometric combination of oblique views from the gyrocopter also resulted in vertical
591 precision being slightly better than the horizontal component. Over the region of
592 interest, the interpolated precision maps showed point precision magnitudes <0.15 m
593 (Figure 9) and strong local variability that dominated any broader structural survey
594 variations. The areas of poor precision correspond to areas of vegetation (compare
595 Figure 9a and b), and resulted from the fewer observations made for points in these
596 areas (Figure 9c and f).

597 With the 2014 SfM and TLS surveys being effectively simultaneously acquired,
598 differences between them should fall appropriately within the estimated confidence
599 bounds. Straightforward DoD comparison shows systematic differences which
600 highlight east to north-east facing steep gully walls, and are indicative of horizontal
601 error in the relative georeferencing of the surveys (Figure 10a). Using a survey-wide
602 $LoD_{95\%}$ retained these systematic significant differences, due to horizontal error
603 remaining neglected (Figure 10b).

604 With 3-D analysis using native M3C2 algorithm, nearly all the differences
605 between the surfaces fall within the large uncertainty dominated by the rather
606 conservative *reg* term (Figure 10c). Using the precision maps adaptation, M3C2-PM,

607 more regions of significant difference were highlighted (Figure 9d), but nevertheless,
608 the approach substantially reduced the effects of horizontal error (c.f. Figure 10b).
609 Many of the areas where differences exceeded the local 3-D LoD_{95%} are located at
610 the bottoms of gullies and their tributaries, and have been previously identified as the
611 least accurate in the SfM survey (Smith and Vericat, 2015), and could potentially
612 have been affected by smoothing during the dense image matching stage.

613 *Predicted survey performance under direct georeferencing*

614 Reprocessing the 2014 SfM survey to simulate direct georeferencing showed
615 that, over the area of interest, similar point precisions could be achieved when the
616 prescribed camera position precision was similar to that of the GCP field
617 measurements (Figure 11). However, knowing camera positions more precisely gave
618 little gain, because photogrammetric considerations, such as image measurement
619 precision of tie points, were the limiting factor (i.e. just as in Figure 1b). To
620 understand the best possible precision that could be achieved with the images, the
621 survey was also processed by removing all control data prior to a bundle adjustment,
622 to give an ‘inner constraints’ adjustment which provides precision values within a
623 local coordinate system defined by the initial coordinate values of the tie points
624 alone, (i.e. Figure 1a). This resulted in a mean vertical point precision of 23 mm, with
625 10% and 90% bounds of 8 and 50 mm (the grey band, Figure 11). Thus, when
626 including control measurements in order to georeference the survey, deviations from
627 this optimum can be considered as dilution of the achievable precision due to the
628 introduction of control that is weaker than the underlying tie point photogrammetry
629 (i.e. as in Figure 1c).

630 Weakening the camera position precision led to degraded 3-D point precision,
631 reflecting a weak overall georeferencing (Figure 11, in the same manner as

632 illustrated in Figures 1c and 7c, d). The same effect was shown for GCP-based
633 georeferencing (Figure 11) but, with more camera positions (and more broadly
634 distributed) than GCPs, then overall point precision was less sensitive to control
635 measurement precision under direct georeferencing. For direct georeferencing,
636 control measurement precision became an overall limiting factor at weaker control
637 precision values than for GCP georeferencing. Furthermore, once point precision
638 was limited by control measurement, point precision was approximately three times
639 better from direct georeferencing than from using GCPs (Figure 11).

640 *Change detection with 3-D precision maps*

641 Changes between the 2014 and 2015 surveys (Figure 12, Table 5) were greatest
642 when calculated by straightforward DoD (Figure 12a), which showed a general sub-
643 decimetre lowering of the surface between 2014 and 2015, but with some systematic
644 height increases associated with steeper slopes, indicative of error in the relative
645 horizontal registration of the two surveys. Using a single survey-wide $LoD_{95\%}$
646 accommodated much of the overall lowering within the estimate of measurement
647 precision, but notable areas of systematic height increase remained (Figure 12b).

648 In contrast, the native M3C2 algorithm identified only a very few areas where
649 change exceeded the local 3-D $LoD_{95\%}$ value (Figure 12c), giving results that are out
650 of step with field observations of active sediment transport through the main
651 thalwegs of the study area. Finally, the M3C2-PM approach (Figure 12d) delivered
652 the most plausible distribution of topographic change of the methods tested, with
653 minimal areas of apparent upward change resulting from unaccounted-for horizontal
654 error on steep slopes, and volume losses dominantly restricted to gully bottoms and
655 tributaries.

656 Discussion

657 Our results have indicated that considering 3-D precision improves change
658 detection in areas of complex topography. The detected pattern of sediment loss
659 within the badland catchment is very similar to that observed in TLS data over the
660 previous year (i.e. between 2013 and 2014, see Smith and Vericat, 2015); however,
661 the calculated average topographic change of -18.2 mm a^{-1} (Table 5) is far greater
662 than that calculated for 2013 to 2014 (-1.44 mm a^{-1}). With sediment erosion and
663 transport in badlands known to be concentrated in individual high-magnitude rainfall
664 events (e.g. Cantón, *et al.*, 2001), analysis of the rainfall record confirms that the
665 2014 to 2015 monitoring period exhibited six storms of a greater intensity ($\sim 40 \text{ mm}$
666 hr^{-1} over a 15 minute interval) than any in the previous year. Moreover, when
667 converted to sediment yield ($272 \text{ t ha}^{-1}\text{a}^{-1}$ over a 0.471 ha area) it is in line with
668 erosion rates measured elsewhere in Mediterranean badlands (Nadal-Romero, *et al.*,
669 2011). Thus, 3-D precision maps facilitate robust geomorphological analysis and
670 could be used to design survey campaigns that achieve specific $\text{LoD}_{95\%}$ values
671 across an area. They also provide insight into the factors behind precision variability
672 between and within surveys, and can indicate whether photogrammetric or
673 georeferencing aspects are overall limiting factors.

674 *Interpreting precision maps*

675 Point precision is affected by range of factors that we have considered as either
676 'photogrammetric' (i.e. internal to the photogrammetric network, such as imaging
677 geometry and the quality of the tie point identification within the images, Figure 1a)
678 or related to the georeferencing (e.g. the external control measurements which limit
679 precision in Figure 1c).

680 Precision maps showing broad, systematic variations (e.g. Figure 6c, d) indicate
681 weakness in overall survey georeferencing (i.e. as Figure 1c), symptomatic of weak
682 control. This can either be due to the poor precision of control measurements, or
683 because control is poorly distributed (e.g. too few, or insufficiently spaced, control
684 measurements). For an imaging geometry appropriate to aerial surveys, the
685 degradation in precision away from the centroid of control measurements (Figure 6c,
686 d) is likely to dominantly reflect uncertainty in the rotational component of overall
687 georeferencing, and indicate the probability of slope error in a DEM (e.g.
688 Carbonneau and Dietrich, 2016). More control, or control more widely distributed or
689 measured to better precision, will improve overall rotational georeferencing precision,
690 and may result in uncertainty in scale and translational components dominating point
691 precision estimates. Forecasting improvements in rotation and scale will not be
692 straightforward and will depend on the quality, locations and number of additional
693 measurements. In contrast, and based on straightforward error statistics (e.g.
694 Borradaile, 2003), translational precision should approximate to $n^{-1/2}$ of the control
695 measurement precision, where n is the number of control measurements.

696 If precision maps indicate strong localised variations, then photogrammetric
697 factors are being expressed, e.g. differences in image measurement quality for
698 individual tie points, and image network geometry aspects such as image overlap
699 and convergence (e.g. Figure 6a, and badlands survey, Figure 9b). Weak precision
700 will result from small numbers of observations for a point, from similar positions (i.e.
701 narrow angles of ray convergence); image matching can be hindered by too large
702 separation of images. Thus, such variations can highlight areas of poor image
703 coverage (e.g. resulting from partial occlusions in complex terrain), or regions of
704 more challenging image matching, such as due to vegetation (Figure 9a, b).
705 Identifying these areas through carrying out a preliminary survey would enable

706 enhanced survey designs to ensure precision requirements can be met across the
707 full area.

708 For the badlands survey, overall point precision over the full extent of the sparse
709 point cloud was limited by the control, due to GCP deployment being spatially
710 restricted to the central region of interest (Figure 5). However, within the area of
711 interest, the GCPs provided strong constraints, and variations in point precision
712 reflected local differences in the number (and probably quality) of image
713 observations per point. Weak matching in zones of vegetation resulted in the areas
714 of worst precision, and error ellipses indicated precision differences due to the
715 complex topography being viewed from different directions. With the control
716 measurements not being the limiting factor over the region of interest, fewer GCPs
717 could have been used without substantial effect on overall point precisions. Using
718 the Monte Carlo analysis of James, *et al.* (2017), specifically aimed at analysing
719 GCP performance and identifying minimum numbers, indicated that survey quality
720 would be maintained with only 8 GCPs. This figure is in line with the current work
721 where, for a mean GCP measurement precision of 26 mm, 8 GCPs would provide a
722 translational precision of <10 mm, so (assuming the GCPs were suitably distributed)
723 overall survey precision would remain limited by photogrammetric considerations
724 (Figure 11).

725 *Direct georeferencing versus GCPs*

726 Photogrammetric best practice recommends that control measurements are
727 distributed across and surrounding the volume encompassing the survey area
728 (Luhmann, *et al.*, 2006). When using GCPs, tie and control points are ground-based
729 and the influence of control on the interpretation of precision maps is relatively
730 straightforward to consider (as described above) because the control is in close

731 proximity to the surveyed points. Note that the effects of GCP precision and
732 distribution on survey quality have been well studied within conventional aerial
733 photogrammetry (Krauss, 1993). For direct georeferencing of typical aerial surveys,
734 the use of camera positions as control displaces the control measurements above
735 the survey volume. In this case, positional error can be effectively magnified within
736 the survey region due to the effects of angular uncertainty in overall georeferencing
737 being enhanced along the observation distance. This issue reduces as the span over
738 which images are acquired increases with respect to the observation distance, i.e. as
739 the distance along or across imaging flight paths increases, with respect to the flying
740 height. Thus, for direct georeferencing, with all other things equal, wider flight
741 patterns, capturing convergent imaging of a central, localised region (as in the
742 badlands case study, Figure 5d) would be recommended (Figure 13).

743 To improve precision when direct georeferencing, capturing more images
744 represents an efficient way to acquire more control measurements. In the
745 simulations and case study here, there were ~4–8 times more images than GCPs.
746 Thus, in line with the $n^{-1/2}$ argument and for equally precise control measurements,
747 survey precision under direct georeferencing could be 2–3 times better than from
748 GCP-control (e.g. Figure 11). Alternatively, camera positions could be measured to
749 approximately only half to a third of the quality of the GCPs, to achieve a similar
750 overall point precision. This could be diluted further if more images were acquired,
751 albeit with diminishing returns; it may be feasible to improve precision by an order of
752 magnitude through capturing 100 rather than 10 images, but the ~1000 images
753 required for another order of magnitude improvement could have disadvantages for
754 practical image acquisition and rapid data processing. Nevertheless, in most cases,
755 camera position cannot be measured as precisely as a ground point due to the
756 specific GPS (or other) measurement technologies involved, thus, acquiring more

757 images is likely to be a useful strategy for direct georeferencing deployments.
758 Improving the georeferencing will enable the overall survey precision to be enhanced
759 up to the point that precision becomes limited by the photogrammetric considerations
760 (i.e. imaging geometry, quality of the tie points etc.) rather than the control
761 measurements (such as for the GCP-case illustrated in Figure 1b).

762 In this work, the use of only camera positions in direct georeferencing has been
763 explored, but measurements of camera orientation can also be included in the
764 process (e.g. Cramer, *et al.*, 2000). However, in the GCP-georeferenced badlands
765 survey, the processed image network provided camera rotations with precision
766 estimates of order 10^{-2} degrees (Table 3), which is approximately two orders of
767 magnitude better than delivered by current UAV-suitable orientation sensors
768 (Gabrlik, 2015; Pfeifer, *et al.*, 2012). Thus, first indications are that practical
769 measurements of camera orientation may not currently be able to add to the quality
770 of the results. Nevertheless, due to the interdependencies between camera position
771 and orientation within photogrammetric processing, the precision of derived values is
772 no guarantee of the effectiveness of using measurements as control, and including
773 orientation data could be an area for further research. As an example of such
774 complexity, it is interesting to note that using camera positions as control appeared
775 more effective at mitigating the doming error than GCPs, even when the GCPs were
776 measured with twice as good precision (compare the 'Shape' plots in Figure 6a and
777 7a).

778 For the badlands survey, the camera locations widely bracketed the region of
779 interest (Figure 5), reducing the influence of rotational components of overall
780 georeferencing uncertainty on point precision. Thus, for direct georeferencing using
781 poor precision camera positions, point precision may be expected to reflect
782 translational uncertainty, with magnitudes approximating to $n^{-1/2} \times$ camera position

783 precision. This is shown for camera position precision values exceeding ~200 mm
784 (Figure 11), where (for 104 images) mean point precisions approach ~0.1 × camera
785 position precision. Thus, directly georeferencing the survey using multi-metre
786 precision camera position measurements (typical of a consumer UAV) would have
787 resulted in multi-decimetre point precision, but using camera position observations
788 known to ~0.1 m would be expected to achieve similar overall precision as from the
789 GCP array.

790 In contrast, for GCP-based georeferencing under sufficiently weak control that it
791 limited overall survey precision, then rotational georeferencing components formed
792 an import contribution to dilute point precision, due to the GCP distribution being
793 more spatially restricted than the camera positions. Consequently, mean point
794 precision values did not approach the $n^{-1/2}$ × control precision limit (the uppermost
795 dashed line for 19 control points in Figure 11).

796

797 *Camera models, parameter correlations and quality control*

798 The additional camera parameter precision and correlation information provided
799 either by the Monte Carlo approach (or now directly available within the most recent
800 version of PhotoScan v.1.2.6) promotes rigorous quality assessment of self-
801 calibrating image networks through enabling good practice checks. For topographic
802 surveys, these checks should be carried out before the dense matching (MVS) in an
803 SfM-based workflow:

- 804 1) All camera parameters included in the camera model should improve the results
805 (i.e. their use in the camera model should reduce RMS image residuals and check
806 point discrepancies).

807 2) All camera parameter magnitudes should exceed the precision to which they are
808 determined. Parameters that fail this test, or have a magnitude of the same order
809 as their precision, should have their value fixed at zero (i.e. the parameter is
810 inactive and removed from optimisation) and the self-calibration analysis run again
811 (e.g. Granshaw, 1980).

812 3) Camera parameters should be checked for high magnitude correlations between
813 them (i.e. Table 4). Strong correlations between camera parameters are likely to
814 indicate weakness in the image network that result in the relative effects of the
815 different parameters being inseparable. Where such strong correlations exist, the
816 importance of the parameter pair can be tested by observing whether results
817 deteriorate if one of the parameters is removed from the optimisation. If they do,
818 the parameter can be reinstated, but if not, then it can be fixed at zero to avoid
819 over-parameterisation of the camera model. Note that radial distortion parameters
820 are expected to be strongly correlated (Clarke and Fryer, 1998; Tang and Fritsch,
821 2013); nevertheless, two are likely to be useful for most consumer cameras (for a
822 detailed analysis, see Wackrow, *et al.* (2007)).

823 4) Alongside checks for images with systematic or large magnitude tie point image
824 residuals (James, *et al.*, 2017), camera orientation (precision in position and
825 direction) can be used to test for poorly constrained images. Photographs that
826 show anomalously weak orientations can be considered for removal from the
827 network, because they will not be adding to the strength of the network, and may
828 be contributing to surface error.

829 *Integrating precision into DEM uncertainty processing*

830 Precision maps represent a valuable tool for propagating spatially variable
831 precision in modern SfM surveys forward into established uncertainty-based DEM

832 workflows. Although we use a fully 3-D method for change detection, our interpolated
833 precision maps are also well placed for direct integration with conventional 2.5-D
834 DEM processing. Such an approach may be suitable in areas where topography is
835 sufficiently flat that horizontal precision components may be neglected. However,
836 with precision estimates underpinned by Gaussian statistics, they could be optimistic
837 in some difficult field scenarios. In these cases, precision information can be
838 considered within existing approaches based on fuzzy inference, along with other
839 information such as orthoimage colour or texture to enhance the spatial context (e.g.
840 Wheaton, *et al.*, 2010). Thus, precision maps should form a first step from which
841 other uncertainties inherent within DEM processing (e.g. Wechsler, 2007) can also
842 be considered.

843 **Conclusions**

844 SfM-based surveys are increasingly facilitating routine acquisition of high
845 resolution topographic models, and are transforming data collection practices across
846 environmental and geomorphological research. However, with this, and with
847 photogrammetric processing usually concealed within 'black box' software, the
848 requirement for greater understanding of the associated uncertainties becomes more
849 pressing. Our robust 3-D detection of topographic change is built on precision maps
850 that also facilitate understanding of the fundamental survey characteristics that affect
851 measurements. Such understanding is vital for optimising future work through
852 improving survey planning and for more informed decision-making for GCP
853 deployment or the use of direct georeferencing. By providing access to the metrics
854 that are routinely used for network quality control in metric photogrammetry (such as
855 camera parameter precisions, correlations and point error ellipsoids), our Monte
856 Carlo approach offers a substantial advance for rigorous topographic measurement

857 using SfM. Although the Monte Carlo analysis requires several thousand bundle
858 adjustments, the subsequent dense matching is likely to remain the slowest stage
859 within a complete workflow. Hopefully, future SfM software will both integrate and
860 expose rigorous precision analysis (as PhotoScan v.1.2.6 now does for camera
861 parameters), and precision maps will become a standard component of topographic
862 models and subsequent processing. By applying our method, we show that:

863 1) In areas of complex topography and steep slopes, estimates of sediment budget
864 from photo-based surveys can be substantially improved by considering the 3-D
865 and spatially variable survey precision, when deriving confidence intervals for
866 change detection.

867 2) Such analyses are enabled by 3-D precision maps which integrate the
868 photogrammetric and georeferencing contributions to photo-based survey
869 precision. The interpretation of precision maps gives insight into the precision-
870 limiting factors, thus, a simulation or analysis of a preliminary survey is
871 recommended to optimise survey design.

872 3) Precision estimates that vary smoothly across a survey (e.g. Figure 6c, d and 7c,
873 d) indicate that control measurements are the dominant factor (Figure 1c) and
874 that survey precision could be improved through enhanced survey control (e.g.
875 more GCPs or better measured camera positions, Figure 13b, c). When
876 rotational components of georeferencing are not contributing substantially to
877 point precisions, then overall point precision may be estimated as $n^{-1/2} \times$ control
878 precision (Figure 11).

879 4) If precision maps show details that reflect characteristics such as changes in
880 image overlap (e.g. Figure 6c, d and 7c, d) or surface features such as
881 vegetation (e.g. Figure 5) then survey precision is being dominated by

882 photogrammetric considerations. In this case, improving control is unlikely to be
883 worthwhile, but gains are likely to be made by improving image measurements
884 (e.g. removing tie points with few observations or with large image residuals) or
885 by strengthening the image network geometry (Figure 13a).

886 As the use of SfM-based techniques in geomorphology matures, there will be
887 increased demand for the characteristic ease of data capture and flexibility of SfM
888 software to be combined with the rigorous uncertainty estimates exemplified by
889 traditional photogrammetry. Precision maps and 3-D confidence-bounded surface
890 change detection through M3C2-PM facilitate the use of such photogrammetric
891 uncertainty estimates in a geomorphology context, and our Monte Carlo approach
892 provides this capability for current SfM workflows.

893 **Acknowledgements**

894 We thank Damià Vericat for providing the TLS data and for fieldwork assistance.
895 Dimitri Lague and Trevor Page are gratefully acknowledged for discussions on M3C2
896 and uncertainty respectively. Badland surveys are supported by grants from the
897 British Society for Geomorphology, embedded within the framework of MorphSed, a
898 research project funded by the Spanish Ministry of Economy and Competiveness
899 and the European Regional Development Fund (CGL2012-36394). We thank the
900 Associate Editor, A. Eltner and an anonymous reviewer for highly constructive
901 comments that have helped clarify the manuscript throughout.

Figures

902
903
904
905
906
907
908
909
910
911
912
913
914
915
916
917
918
919
920
921
922
923
924
925
926
927

Figure 1. Survey precision and georeferencing; all panels are purely illustrative 2-D sketches only. (a) Processing photo-based surveys enables the positions of tie points (black circles) to be determined on the topographic surface (dark grey line) through observing the points in different images. Uncertainty in the tie point positions can be represented by error ellipsoids (enlarged for visibility) which, through their size and orientation, reflect the different contributions to photogrammetric uncertainty, such as the network geometry and image measurement precision. Overall, the tie point uncertainties result in uncertainty within the shape of the derived surface, as illustrated by the light grey bands surrounding the darker grey line. (b) When the survey is georeferenced (e.g. through the inclusion of GCPs as control measurements, shown by black ellipses) precision is given in the geographic coordinate system. If control precision is better than the precision from the photogrammetry (i.e. better than in (a)), then precision estimates retain the variations due to the underlying photogrammetric considerations. (c) However, if control is weak (e.g. GCPs are measured to poor precision) then precision in the geographic coordinate system can become limited by the control measurements. The surface will retain the shape derived by the tie point photogrammetry (i.e. in (a)), but its transform into geographic coordinates will effectively be subject to large uncertainties in scale, translation and rotation.

Figure 2. Schematics of the flight path and image footprints for the simulated UAV surveys. (a) Flight paths are illustrated using dark blue cones to show the locations of image acquisitions along twin sets of parallel flight lines. Red cones show the positions of additional acquisitions for simulations that involved two gently banked

928 turns to include oblique (20° to the vertical) imagery (see Table 1 and James and
929 Robson (2014a) for details). (b) Corresponding image footprints, with black triangles
930 indicating GCP locations.

931

932 **Figure 3.** Workflow for confidence-bounded 3-D change detection with SfM surveys
933 and precision maps. See Figure 4 for further details on the M3C2-PM approach.

934

935 **Figure 4.** Change detection in photogrammetric point clouds with M3C2-PM. Steps 1
936 and 2 represent use of the M3C2 algorithm (Lague, *et al.*, 2013) to identify local
937 normal directions between point clouds and determine the local mean separation
938 distance in this direction, L_{M3C2} . In Step 3, the adapted M3C2-PM approach uses
939 photogrammetric precision estimates to derive a confidence interval (or LoD) for this
940 distance measurement. Each mean point, i_1 and i_2 , is associated with precision
941 estimates in the X , Y and Z directions, representing an error ellipsoid. The
942 confidence interval for distance measured in the normal direction, \mathbf{N} , is then
943 determined using the components of precision in that direction, σ_{N1} and σ_{N2}
944 (Equation 2). Redrawn in part from Lague, *et al.* (2013).

945

946 **Figure 5.** The 2014 badlands survey. (a, b) Examples of the aerial images captured
947 with the inset (80 × 50 pixels) showing a GCP target. From the ground, an example
948 eroding headcut (c) shows the high local relief and steep slopes, with the influence of
949 differing compactness within the structured Eocene marl sequence being apparent
950 on the surface form (for scale, the square red targets are 200 × 200 mm). (d) A
951 perspective view of the rendered topographic model and camera positions, showing
952 the wider distribution of tie points. (e) The associated DEM visualised by hill-shade

953 and overlaid with GCP positions (note that 4 GCPs were outside this extent);
954 triangles for control points, and circles for check points.

955

956 **Figure 6.** Precision and vertical error maps for simulated UAV surveys
957 georeferenced using GCPs. Four survey scenarios, represented by the rows, are
958 characterised by strong (a, b) or weak (c, d) ground control (Table 1, with ‘strong’
959 control representative of using dGPS-measured targets as GCPs), and the inclusion
960 (b, d) or not (a, c) of banked turns in the flight plan (Figure 2). GCP locations are
961 indicated by the triangle symbols and the inset value in the top right of each
962 precision plot gives the mean tie point precision (in mm) within the region
963 encompassed by the dashed line in (a). Error contributions were determined by
964 deriving, then applying the Helmert transform that best-fitted the processed points to
965 their initial, simulated positions. The overall georeferencing error component is then
966 the change in point coordinates given by the Helmert transform, and the surface
967 shape error is given by the remaining discrepancies. Note that only vertical
968 components are shown.

969

970 **Figure 7.** Precision and vertical error maps for simulated UAV surveys directly
971 georeferenced using camera position coordinates. The four survey scenarios,
972 represented by the rows, are characterised by strong (a, b) or weak (c, d)
973 georeferencing (as determined by the simulated precision of camera position
974 measurements, with ‘weak’ representative of data from a consumer-grade UAV,
975 Table 1), and the inclusion (b, d) or not (a, c) of banked turns in the flight plan
976 (Figure 2). Note the one to two orders of magnitude differences between the colour
977 scales of the weak and strong scenarios. The value inset in the top right of each
978 precision plot gives the mean tie point precision (in mm) within the region

979 encompassed by the dashed line in (a), for comparison with Figure 6. Surface error
980 was calculated just as for Figure 6.

981

982 **Figure 8.** (a) Variability in SfM-Monte Carlo tie point precision estimates as a
983 function of the number of iterations in the Monte Carlo analysis. Each plotted line
984 shows the difference in estimated precision for a tie point, from the final estimate for
985 that point made after 4,000 iterations. (b) Estimates of point coordinate precision
986 components in X, Y and Z, as determined from the SfM-Monte Carlo approach (with
987 4,000 iterations) are validated by their correspondence with those provided directly
988 by least squares bundle adjustment in VMS (each plotted symbol represents the
989 precision estimate for one tie point). Grey lines represent 1:1 ratios for visual
990 reference.

991

992 **Figure 9.** Precision maps for the 2014 badlands survey. The survey orthomosaic (a)
993 gives spatial reference for the summary map of precision magnitude (b), as
994 interpolated from tie points (the inset text gives the mean value). Excerpts of typical
995 image texture (300 × 300 pix) show that bare topography can provide good precision
996 (blue) and that areas of weakest precision (yellow) mostly reflect vegetation cover.
997 (c) The tie point locations used for map construction, coloured by the number of
998 images in which each point has been observed (note the \log_{10} colour scale). The
999 underlying point precision data can be provided as X, Y and Z components, shown
1000 by histograms (d, with inset mean values), precision maps (e), or by a 3-D error
1001 ellipsoid for each point. Projecting error ellipsoids on a cross section (f, for points
1002 within 1 m of the section A-A' in (a-c)), underscores that the weakest points are
1003 derived from few, and generally oblique, observations.

1004

1005 **Figure 10.** Vertical differences between the 2014 TLS and SfM-based surveys
1006 determined using different methods for comparison. All plots are cropped to remove
1007 areas of vegetation and are given at a horizontal resolution of 0.1 m, overlying a hill
1008 shade image. In areas where change is determined to be significant, vertical change
1009 is overlain in colour. (a) Straightforward DEM of difference. (b) As (a), but
1010 transparent where DoD values are smaller than an LoD_{95%} of 78 mm. (c and d) As
1011 (a), but showing only areas where the original point clouds were detected to be
1012 significantly different by M3C2 (c) or M3C2-PM (d).

1013

1014 **Figure 11.** Tie point precision statistics for the region of interest of the badlands
1015 survey, for different assumed values of mean control measurement precision. Mean
1016 point precision values (symbols) are bracketed by 10th and 90th percentile bars. For
1017 direct georeferencing (using camera positions as control measurement), the
1018 overlying symbols illustrate that the PhotoScan results are almost indistinguishable
1019 from those from VMS. All results for GCP-georeferencing were processed with
1020 PhotoScan only, using the selected GCPs indicated in the underlying distribution
1021 maps as control. The results associated with dashed bars are for the GCP precision
1022 values of the field data. The dashed horizontal line (mean) and grey band (10th and
1023 90th percentiles) give the point precision derived in the absence of any control
1024 measurements (i.e. Figure 1a). This ‘inner constraints’ bundle adjustment indicates
1025 the best point coordinate precision that could be achieved with this survey’s tie point
1026 image measurements and image network geometry. The inclined long-dashed lines
1027 represent point position precisions of $n^{-1/2} \times$ control measurement precision, for $n = 19$
1028 (upper line, reflecting 19 GCPs) and $n = 104$ (lower line, reflecting the number of
1029 camera positions).

1030

1031 **Figure 12.** Vertical change between the 2014 and 2015 SfM-based surveys
1032 determined using different methods for comparison. All plots are cropped to remove
1033 areas of vegetation and are given at a horizontal resolution of 0.1 m, overlying a hill
1034 shade image. In areas where change is determined to be significant, vertical change
1035 is overlain in colour. (a) Straightforward DEM of difference. (b) As (a), but
1036 transparent where DoD values are smaller than an $LoD_{95\%}$ of 80 mm. (c and d) As
1037 (a), but showing only areas where the original point clouds were detected to be
1038 significantly different by M3C2 (c) or M3C2-PM (d).

1039

1040 **Figure 13.** Schematic illustration of factors in precision-based planning of UAV
1041 missions based on (a) photogrammetric considerations, or control (georeferencing)
1042 characteristics for (b) GCP-georeferenced and (c) directly georeferenced surveys.
1043 Triangles represent camera positions and orientations, above a grey-shaded
1044 topography. Ellipses indicate control measurements, either of GCPs or camera
1045 positions, with their relative size indicative of the relative precision magnitude.

1046

1047

1048

References

- 1049 Bláha M, Eisenbeiss H, Grimm D, Limpach P. 2011. Direct georeferencing of UAVs.
1050 International Archives of Photogrammetry and Remote Sensing and Spatial
1051 Information Sciences **XXXVIII-1/C22**: 131-136
- 1052 Borradaile GJ. 2003. Statistics of Earth Science Data : their distribution in space,
1053 time, and orientation. Springer-Verlag Berlin: Heidelberg
- 1054 Brasington J, Langham J, Rumsby B. 2003. Methodological sensitivity of
1055 morphometric estimates of coarse fluvial sediment transport. *Geomorphology*
1056 **53**: 299-316. DOI: 10.1016/S0169-555x(02)00320-3
- 1057 Cantón Y, Domingo F, Solé-Benet A, Puigdefábregas J. 2001. Hydrological and
1058 erosion response of a badlands system in semiarid SE Spain. *Journal of*
1059 *Hydrology* **252**: 65-84. DOI: 10.1016/s0022-1694(01)00450-4
- 1060 Carbonneau PE, Dietrich JT. 2016. Cost-Effective non-metric photogrammetry from
1061 consumer-grade sUAS: Implications for direct georeferencing of structure from
1062 motion photogrammetry. *Earth Surface Processes and Landforms*: in press.
1063 DOI: 10.1002/esp.4012
- 1064 Casella E, Rovere A, Pedroncini A, Mucerino L, Casella M, Cusati LA, Vacchi M,
1065 Ferrari M, Firpo M. 2014. Study of wave runup using numerical models and
1066 low-altitude aerial photogrammetry: A tool for coastal management. *Estuarine*
1067 *Coastal and Shelf Science* **149**: 160-167. DOI: 10.1016/j.ecss.2014.08.012
- 1068 Castillo C, Pérez R, James MR, Quinton NJ, Taguas EV, Gómez JA. 2012.
1069 Comparing the accuracy of several field methods for measuring gully erosion.
1070 *Soil Science Society of America Journal* **76**: 1319-1332. DOI:
1071 10.2136/sssaj2011.0390

1072 Chandler J. 1999. Effective application of automated digital photogrammetry for
1073 geomorphological research. *Earth Surface Processes and Landforms* **24**: 51-63

1074 Chiang K-W, Tsai M-L, Chu D-H. 2012. The Development of an UAV borne direct
1075 georeferenced photogrammetric platform for ground control point free
1076 applications. *Sensors* **12**: 9161-9180. DOI: 10.3390/s120709161

1077 Chu H-J, Chen R-A, Tseng Y-H, Wang C-K. 2014. Identifying LiDAR sample
1078 uncertainty on terrain features from DEM simulation. *Geomorphology* **204**: 325-
1079 333. DOI: 10.1016/j.geomorph.2013.08.016

1080 Clarke TA, Fryer JG. 1998. The development of camera calibration methods and
1081 models. *Photogrammetric Record* **16**: 51-66. DOI: 10.1111/0031-868x.00113

1082 Cooper MAR, Robson S. 1996. Theory of close range photogrammetry. In *Close*
1083 *range photogrammetry and machine vision*, Atkinson KB (ed). Whittles
1084 Publishing: Caithness; 9-51.

1085 Cramer M, Stallmann D, Haala N. 2000. Direct georeferencing using GPS/inertial
1086 exterior orientations for photogrammetric applications. *International Archives of*
1087 *the Photogrammetry, Remote Sensing and Spatial Information Sciences*
1088 **XXXIII, Part B3**: 198-205

1089 Dietrich JT. 2016. Riverscape mapping with helicopter-based Structure-from-Motion
1090 photogrammetry. *Geomorphology* **252**: 144-157. DOI:
1091 10.1016/j.geomorph.2015.05.008

1092 Eling C, Wieland M, Hess C, Klingbeil L, Kuhlmann H. 2015. Development and
1093 evaluation of a UAV based mapping system for remote sensing and surveying
1094 applications. *International Archives of Photogrammetry, Remote Sensing, and*
1095 *Spatial Information Sciences* **XL-1/W4**: 233-239. DOI: 10.5194/isprsarchives-
1096 XL-1-W4-233-2015

1097 Eltner A, Baumgart P, Maas HG, Faust D. 2015. Multi-temporal UAV data for
1098 automatic measurement of rill and interrill erosion on loess soil. *Earth Surface*
1099 *Processes and Landforms* **40**: 741-755. DOI: 10.1002/esp.3673

1100 Eltner A, Kaiser A, Castillo C, Rock G, Neugirg F, Abellan A. 2016. Image-based
1101 surface reconstruction in geomorphometry - merits, limits and developments.
1102 *Earth Surface Dynamics* **4**: 359-389. DOI: 10.5194/esurf-4-359-2016

1103 Förstner W, Wrobel B, Paderes F, Fraser CS, Dolloff J, Mikhail EM, Rajikietgumjorn
1104 W. 2013. Analytical photogrammetric operations. In *Manual of*
1105 *Photogrammetry*, McGlone JC (ed). American Society for Photogrammetry and
1106 *Remote Sensing*: Bethesda.

1107 Förstner W, Wrobel BP. 2013. Mathematical concepts in photogrammetry. In *Manual*
1108 *of photogrammetry*, McGlone JC (ed). American Society for Photogrammetry
1109 *and Remote Sensing*: Bethesda.

1110 Furukawa Y, Ponce J. 2007. Accurate, dense, and robust multi-view stereopsis. In
1111 *IEEE Conference on Computer Vision and Pattern Recognition (CVPR)*. DOI:
1112 10.1109/CVPR.2007.383246

1113 Gabrlik P. 2015. The use of direct georeferencing in aerial photogrammetry with
1114 micro UAV. *IFAC-PapersOnLine* **48**: 380–385

1115 Gomez-Gutierrez A, Schnabel S, Berenguer-Sempere F, Lavado-Contador F, Rubio-
1116 Delgado J. 2014. Using 3D photo-reconstruction methods to estimate gully
1117 headcut erosion. *Catena* **120**: 91-101. DOI: 10.1016/j.catena.2014.04.004

1118 Gongga-Saholiariliva N, Gunnell Y, Petit C, Mering C. 2011. Techniques for
1119 quantifying the accuracy of gridded elevation models and for mapping
1120 uncertainty in digital terrain analysis. *Progress In Physical Geography* **35**: 739-
1121 764. DOI: 10.1177/0309133311409086

1122 Granshaw SI. 1980. Bundle adjustment methods in engineering photogrammetry.
1123 Photogrammetric Record **10**: 181-207

1124 Hirschmuller H. 2008. Stereo processing by semiglobal matching and mutual
1125 information. IEEE Transactions on Pattern Analysis and Machine Intelligence
1126 **30**: 328-341. DOI: 10.1109/Tpami.2007.1166

1127 Hugenholtz C, Brown O, Walker J, Barchyn T, Nesbit P, Kurcharczyk M, Myshak S.
1128 2016. Spatial accuracy of UAV-derived orthoimagery and topography:
1129 Comparing photogrammetric models processed with direct geo-referencing and
1130 ground control points. Geomatica **70**: 21-30. DOI: 10.5623/cig2016-102

1131 James MR, Robson S. 2012. Straightforward reconstruction of 3D surfaces and
1132 topography with a camera: Accuracy and geoscience application. Journal of
1133 Geophysical Research **117**: F03017. DOI: 10.1029/2011JF002289

1134 James MR, Robson S. 2014a. Mitigating systematic error in topographic models
1135 derived from UAV and ground-based image networks. Earth Surface Processes
1136 and Landforms **39**: 1413-1420. DOI: 10.1002/esp.3609

1137 James MR, Robson S. 2014b. Sequential digital elevation models of active lava
1138 flows from ground-based stereo time-lapse imagery. ISPRS Journal of
1139 Photogrammetry and Remote Sensing **97**: 160-170. DOI:
1140 10.1016/j.isprsjprs.2014.08.011

1141 James MR, Robson S, d'Oleire-Oltmanns S, Niethammer U. 2017. Optimising UAV
1142 topographic surveys processed with structure-from-motion: Ground control
1143 quality, quantity and bundle adjustment. Geomorphology **280**: 51–66. DOI:
1144 10.1016/j.geomorph.2016.11.021

1145 James MR, Varley N. 2012. Identification of structural controls in an active lava
1146 dome with high resolution DEMs: Volcán de Colima, Mexico. Geophysical
1147 Research Letters **39**: L22303. DOI: 10.1029/2012GL054245

1148 Javernick L, Hicks DM, Measures R, Caruso B, Brasington J. 2016. Numerical
1149 modelling of braided rivers with structure-from-motion-derived terrain models.
1150 River Research and Applications **32**: 1071-1081. DOI: 10.1002/rra.2918

1151 Krauss K. 1993. Photogrammetry, Vol. 1, Fundamentals and Standard Processes.
1152 Dümmlers

1153 Lague D, Brodu N, Leroux J. 2013. Accurate 3D comparison of complex topography
1154 with terrestrial laser scanner: Application to the Rangitikei canyon (N-Z). ISPRS
1155 Journal of Photogrammetry and Remote Sensing **82**: 10-26. DOI:
1156 10.1016/j.isprsjprs.2013.04.009

1157 Lallias-Tacon S, Liebault F, Piegay H. 2014. Step by step error assessment in
1158 braided river sediment budget using airborne LiDAR data. Geomorphology **214**:
1159 307-323. DOI: 10.1016/j.geomorph.2014.02.014

1160 Lane SN, James TD, Crowell MD. 2000. Application of digital photogrammetry to
1161 complex topography for geomorphological research. Photogrammetric Record
1162 **16**: 793-821. DOI: 10.1111/0031-868x.00152

1163 Lane SN, Westaway RM, Hicks DM. 2003. Estimation of erosion and deposition
1164 volumes in a large, gravel-bed, braided river using synoptic remote sensing.
1165 Earth Surface Processes and Landforms **28**: 249-271. DOI: 10.1002/esp.483

1166 Lucieer A, de Jong SM, Turner D. 2014. Mapping landslide displacements using
1167 Structure from Motion (SfM) and image correlation of multi-temporal UAV
1168 photography. Progress In Physical Geography **38**: 97-116. DOI:
1169 10.1177/0309133313515293

1170 Luhmann T, Robson S, Kyle S, Harley I. 2006. Close range photogrammetry:
1171 Principles, methods and applications. Whittles, Caitness

1172 Mian O, Lutes J, Lipa G, Hutton JJ, Gavelle E, Borghini S. 2015. Direct
1173 georeferencing on small unmanned aerial platforms for improved reliability and

1174 accuracy of mapping without the need for ground control points. International
1175 Archives of Photogrammetry, Remote Sensing, and Spatial Information
1176 Sciences **XL-1/W4**: 397-402. DOI: 10.5194/isprsarchives-XL-1-W4-397-2015
1177 Milan DJ, Heritage GL, Hetherington D. 2007. Application of a 3D laser scanner in
1178 the assessment of erosion and deposition volumes and channel change in a
1179 proglacial river. *Earth Surface Processes and Landforms* **32**: 1657-1674. DOI:
1180 10.1002/esp.1592

1181 Milan DJ, Heritage GL, Large ARG, Fuller IC. 2011. Filtering spatial error from
1182 DEMs: Implications for morphological change estimation. *Geomorphology* **125**:
1183 160-171. DOI: 10.1016/j.geomorph.2010.09.012

1184 Mosbrucker AR, Major JJ, Spicer KR, Pitlick J. 2017. Camera system considerations
1185 for geomorphic applications of SfM photogrammetry. *Earth Surface Processes
1186 and Landforms*. In press. DOI: 10.1002/esp.4066

1187 Nadal-Romero E, Martinez-Murillo JF, Vanmaercke M, Poesen J. 2011. Scale-
1188 dependency of sediment yield from badland areas in Mediterranean
1189 environments. *Progress In Physical Geography* **35**: 297-332. DOI:
1190 10.1177/0309133311400330

1191 Nolan M, DesLauriers K. 2016. Which are the highest peaks in the US Arctic? Fodar
1192 settles the debate. *The Cryosphere* **10**: 1245-1254

1193 Nolan M, Larsen C, Sturm M. 2015. Mapping snow depth from manned aircraft on
1194 landscape scales at centimeter resolution using structure-from-motion
1195 photogrammetry. *Cryosphere* **9**: 1445-1463. DOI: 10.5194/tc-9-1445-2015

1196 Oksanen J, Sarjakoski T. 2006. Uncovering the statistical and spatial characteristics
1197 of fine toposcale DEM error. *International Journal of Geographical Information
1198 Science* **20**: 345-369. DOI: 10.1080/13658810500433891

- 1199 Pfeifer N, Glira P, Briese C. 2012. Direct georeferencing with on board navigation
1200 components of light weight UAV platforms. International Archives of the
1201 Photogrammetry, Remote Sensing and Spatial Information Sciences **XXXIX-**
1202 **B7**: 487-492
- 1203 Rehak M, Mabillard R, Skaloud J. 2013. A micro-UAV with the capability of direct
1204 georeferencing. International Archives of the Photogrammetry, Remote Sensing
1205 and Spatial Information Sciences **XL-1/W2**: 317-323
- 1206 Ryan JC, Hubbard AL, Box JE, Todd J, Christoffersen P, Carr JR, Holt TO, Snooke
1207 N. 2015. UAV photogrammetry and structure from motion to assess calving
1208 dynamics at Store Glacier, a large outlet draining the Greenland ice sheet.
1209 Cryosphere **9**: 1-11. DOI: 10.5194/tc-9-1-2015
- 1210 Smith MW, Quincey DJ, Dixon T, Bingham RG, Carrivick JL, Irvine-Fynn TDL, Rippin
1211 DM. 2016. Aerodynamic roughness of glacial ice surfaces derived from high-
1212 resolution topographic data. Journal of Geophysical Research-Earth Surface
1213 **121**: 748-766. DOI: 10.1002/2015jf003759
- 1214 Smith MW, Vericat D. 2015. From experimental plots to experimental landscapes:
1215 topography, erosion and deposition in sub-humid badlands from Structure-from-
1216 Motion photogrammetry. Earth Surface Processes and Landforms **40**: 1656-
1217 1671. DOI: 10.1002/esp.3747
- 1218 Tang RF, Fritsch D. 2013. Correlation Analysis of Camera Self-Calibration in Close
1219 Range Photogrammetry. Photogrammetric Record **28**: 86-95. DOI:
1220 10.1111/phor.12009
- 1221 Turner D, Lucieer A, Wallace L. 2014. Direct georeferencing of ultrahigh-resolution
1222 UAV imagery. IEEE Transactions on Geoscience and Remote Sensing **52**:
1223 2738-2745. DOI: 10.1109/Tgrs.2013.2265295

1224 Wackrow R, Chandler JH. 2011. Minimising systematic error surfaces in digital
1225 elevation models using oblique convergent imagery. *Photogrammetric Record*
1226 **26**: 16-31. DOI: 10.1111/j.1477-9730.2011.00623.x

1227 Wackrow R, Chandler JH, Bryan P. 2007. Geometric consistency and stability of
1228 consumer-grade digital cameras for accurate spatial measurement. *The*
1229 *Photogrammetric Record* **22**: 121-134

1230 Wechsler SP. 2007. Uncertainties associated with digital elevation models for
1231 hydrologic applications: a review. *Hydrology and Earth System Sciences* **11**:
1232 1481-1500

1233 Weng QH. 2002. Quantifying uncertainty of digital elevation models derived from
1234 topographic maps. In *Advances in Spatial Data Handling*, Richardson D, van
1235 Oosterom P (eds). Springer Berlin Heidelberg; 403-418.

1236 Westoby MJ, Brasington J, Glasser NF, Hambrey MJ, Reynolds JM, Hassan MAAM,
1237 Lowe A. 2015. Numerical modelling of glacial lake outburst floods using
1238 physically based dam-breach models. *Earth Surface Dynamics* **3**: 171-199.
1239 DOI: 10.5194/esurf-3-171-2015

1240 Wheaton JM, Brasington J, Darby SE, Sear DA. 2010. Accounting for uncertainty in
1241 DEMs from repeat topographic surveys: improved sediment budgets. *Earth*
1242 *Surface Processes and Landforms* **35**: 136-156. DOI: 10.1002/esp.1886

1243 Woodget AS, Carbonneau PE, Visser F, Maddock IP. 2015. Quantifying submerged
1244 fluvial topography using hyperspatial resolution UAS imagery and structure
1245 from motion photogrammetry. *Earth Surface Processes and Landforms* **40**: 47-
1246 64. DOI: 10.1002/esp.3613

1247

1248

1249

Tables

1250

1251

1252

1253

Table 1. Characteristics of the simulated surveys shown in Figure 2.

1254

Survey detail		Values and characteristics			
Camera	Principal dist.	50 mm			
	Image size	4000 × 3000 pix. (pixel pitch 5 μm)			
	Altitude	50 m			
	Ground pix. size	12.5 mm (nominal)			
Flight plan (Figure 2)	Image overlap	60% forward 30% sidelap (within each parallel set)			
	Network geometry	Weak	80 images, collected from two sets of parallel flight lines, oriented at 20° (Figure 6/7 a, c)		
		Strong	An additional 18 images, in two gently banked turns (Figure 6/7 b, d)		
Georeferencing scenarios		Control survey precision (GCPs or camera pos.)		Image measurement precision (pix)	
		horizontal	vertical	GCPs	Tie points
Using GCPs	Strong (Fig. 6a, b)	10 mm	20 mm	0.1	1.0
	Weak (Fig. 6c, d)	50 mm	100 mm	1.0	0.1
Direct georeferencing	Strong (Fig. 7a, b)	20 mm	40 mm	-	0.5
	Weak (Fig. 7c, d)	2 m	4 m	-	0.5

1255

1256

1257
 1258
 1259
 1260
 1261
 1262

Table 2. Characteristics of the 2014 and 2015 badlands surveys.

		2014	2015
<i>Camera</i>			
	Model	Nikon D3100	Nikon D75
Focal length (35-mm equiv.; mm)		28	28
	Image size (pix)	4608 × 3584	6016 × 4016
	Pixel pitch (µm)	5.0	6.0
<i>Survey</i>			
	Overflight design	7–10 oblique overpasses, mutually inclined, nominal altitude of 50 m (Figure 5d)	
	GCP coordination	dGPS, absolute quality available per-point, means: XY: 14 mm, Z: 26 mm	total station, 3-D quality relative to instrument ^a : XY: 10 mm, Z: 5 mm
<i>Processing</i>			
	Number of images processed	104	99
	GCPs (as control, [as check] pts.)	19 [7]	20 [7]
	GCP image precision (pix)	0.50	1.55
	Tie point image precision (pix)	0.89	1.26
RMS discrepancies on GCPs :			
	Control points (X, Y, Z; mm)	55.6, 42.4, 36.8	13.8 14.1 14.3
	Check points (X, Y, Z; mm)	47.5, 54.8, 24.4	5.7 13.4 11.9

1263 ^a Measurement precision reported by the instrument was ~1 mm, values given here
 1264 account for additional uncertainty due to locating the prism over the GCP.
 1265

1266

1267

1268 **Table 3.** Parameters and survey precision characteristics for the 2014 badlands

1269 survey, processed with GCPs as control.

Parameter or characteristic	PhotoScan ^a	VMS ^b
<i>Camera model (Model A)</i>		
<i>Value ± precision</i>		
Principal distance (P.D.; pix)	3786.42 ± 0.16	3786.40 ± 0.12
Principal point CCx	2295.45 ± 0.08	2296.06 ± 0.04
CCy	1570.16 ± 0.13	1569.72 ± 0.08
Radial distortion K ₁	-9.2484×10 ⁻² ± 8.52×10 ⁻⁵	-9.2265×10 ⁻² ± 7.43×10 ⁻⁵
K ₂	3.5033×10 ⁻² ± 3.57×10 ⁻⁴	3.4263×10 ⁻² ± 3.09×10 ⁻⁴
K ₃	3.1925×10 ⁻³ ± 4.51×10 ⁻⁴	4.3945×10 ⁻³ ± 3.62×10 ⁻⁴
<i>Camera orientations</i>		
<i>Mean precision across all cameras</i>		
Position (X, Y, Z; mm)	16.4, 26.2, 30.5	14.4, 22.3, 26.7
Rotation (roll, pitch, yaw; mdeg.)	21.1, 9.0, 9.1	18.2, 8.0, 8.2
<i>Survey overall georeferencing</i>		
<i>Precision</i>		
Translation (X, Y, Z; mm)	2.6, 2.4, 5.6	n./a.
Slope (angles to X, Y, Z axes; mdeg.)	7.5, 17.4, 0.3	n./a.
Scale (%)	0.0072	n./a.
<i>3-D topographic point coordinates</i>		
<i>Mean precision across all points in region of interest</i>		
Precision (X, Y, Z; mm)	18.6, 14.5, 26.1	18.2, 14.2, 25.2
Shape only ^c (X, Y, Z; mm)	18.3, 13.9, 23.3	17.9, 13.8, 23.0
<i>Dimensionless relative precision ratios (full survey)</i>		
Mean precision : max. survey extent	1 : 29,600	1 : 29,600
Mean precision : mean obs. distance	1 : 4,100	1 : 4,100
Mean precision in pixels (XY, Z; pix.)	1.3, 1.1	1.2, 1.1

1270 ^a Precision values determined using Monte Carlo analysis.

1271 ^b VMS used only to run a bundle adjustment on the image network derived by
 1272 PhotoScan. Camera parameter values are given in the convention used in
 1273 PhotoScan.

1274 ^c 'Shape only' precision is determined after accounting for uncertainty in overall
 1275 georeferencing.

1276

1277

1278

1279 **Table 4.** Parameter correlations for the two camera models tested for the 2014
 1280 badlands survey. *CCx* and *CCy* are the principal point coordinates, *P.D.* is the
 1281 principal distance (focal length), K_{1-3} are radial distortion parameters and $P_{1, 2}$ are
 1282 tangential distortion parameters. Underscores highlight correlation magnitudes that
 1283 exceed 0.10 (except those from self-correlation).

	Camera model A						Camera model B							
	<i>CCx</i>	<i>CCy</i>	<i>P.D.</i>	K_1	K_2	K_3	<i>CCx</i>	<i>CCy</i>	<i>P.D.</i>	K_1	K_2	K_3	P_1	P_2
<i>CCx</i>	1.00						1.00							
<i>CCy</i>	-0.05	1.00					-0.05	1.00						
<i>P.D.</i>	-0.09	<u>-0.62</u>	1.00				<u>-0.41</u>	<u>-0.17</u>	1.00					
K_1	-0.03	-0.09	-0.03	1.00			-0.04	0.00	-0.10	1.00				
K_2	0.03	0.08	0.10	<u>-0.96</u>	1.00		0.10	0.01	0.09	<u>-0.96</u>	1.00			
K_3	-0.03	-0.09	-0.07	<u>0.91</u>	<u>-0.98</u>	1.00	-0.07	-0.02	-0.09	<u>0.91</u>	<u>-0.98</u>	1.00		
P_1							<u>0.27</u>	<u>0.19</u>	<u>0.45</u>	-0.06	0.04	-0.03	1.00	
P_2							-0.04	<u>-0.89</u>	<u>0.18</u>	0.02	-0.01	0.00	<u>0.14</u>	1.00

1284

1285

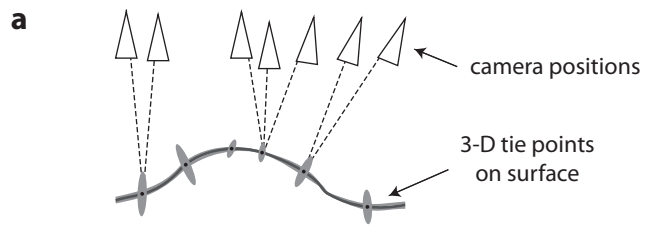
1286

1287 **Table 5.** Sediment budget between 2014 and 2015, calculated using different
1288 methods to determine the regions of detectable change. Average topographic
1289 change was determined using a catchment of 4710 m² and a 1-12 a inter-survey
1290 interval.

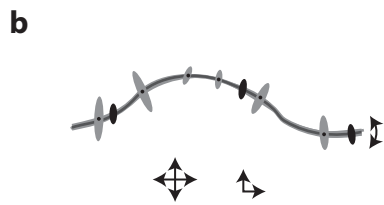
Calculation method used	Total erosion (m ³)	Total deposition (m ³)	Net (m ³)	Average topographic change (mm a ⁻¹)
DoD	-210.49	17.87	-192.61	-36.5
DoD LoD _{95%}	-142.54	8.76	-133.78	-25.4
M3C2	-18.89	0.21	-18.68	-3.5
M3C2-PM	-98.65	2.82	-95.83	-18.2

1291

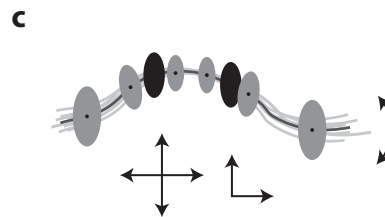
Figure 01



No georeferencing
surface model has shape, but arbitrary scale, translation and rotation with respect to a geographic coordinate system



'Strong' georeferencing
precision limited by photogrammetric considerations; small uncertainties in model scale, translation and rotation



'Weak' georeferencing
precision limited by georeferencing considerations; large uncertainties in model scale, translation and rotation

Figure 02

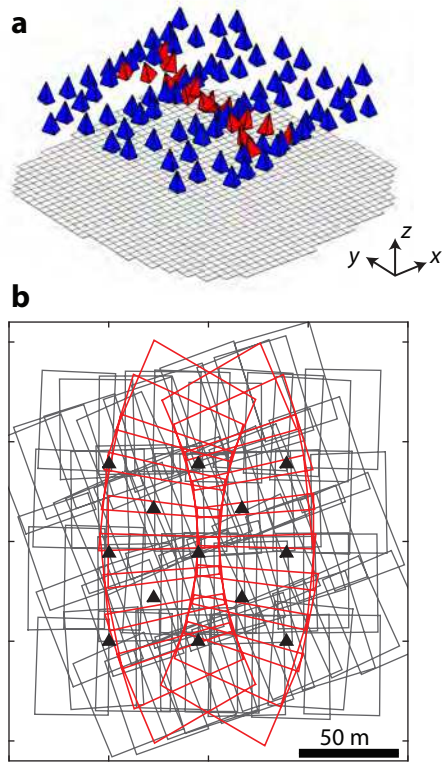


Figure 03

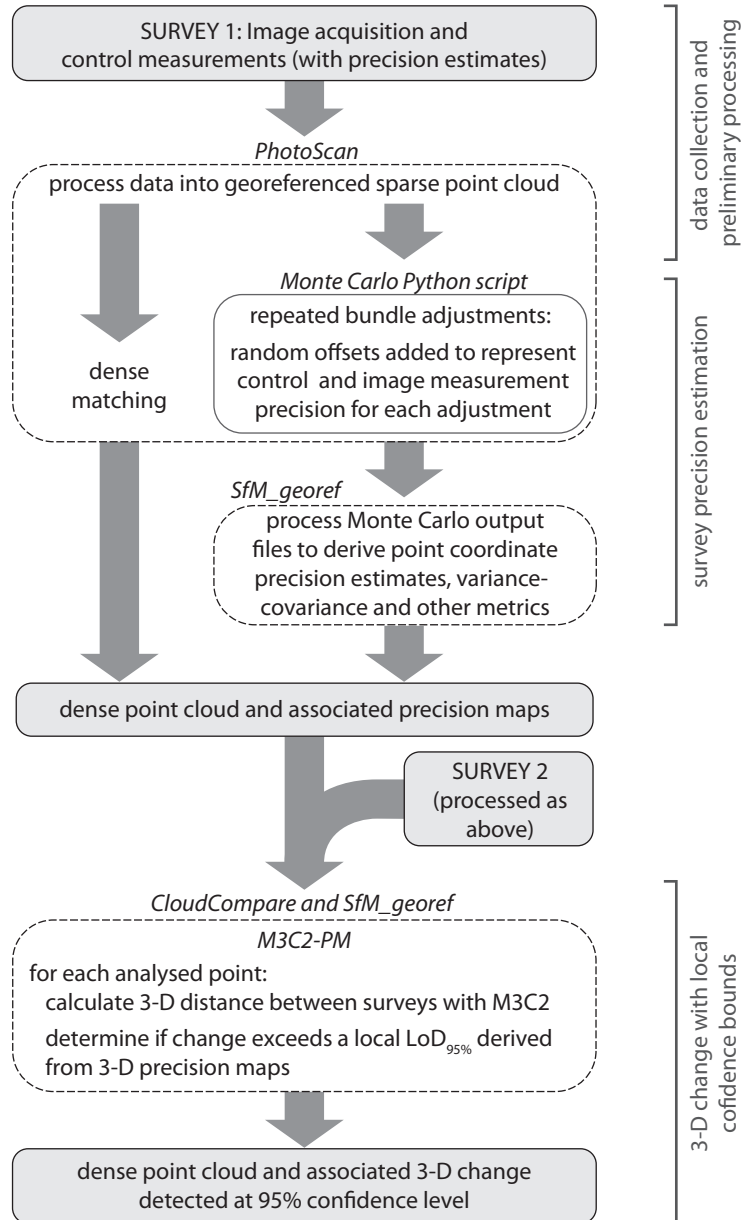
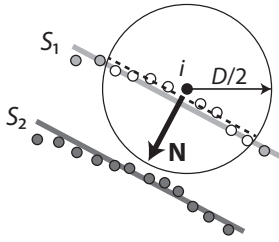
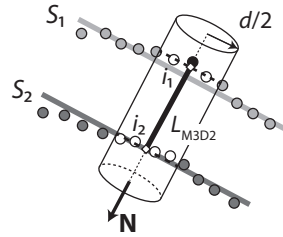


Figure 04

Step 1 (M3C2): Calculation of normal \mathbf{N} at a scale D around the core point i in cloud S_1 .



Step 2 (M3C2): Average distance between the two cloud measured along \mathbf{N} between mean points i_1 and i_2 , derived at a scale d .



Step 3: Position uncertainty for i_1 and i_2 ascertained from precision maps and used to determine distance uncertainty in direction \mathbf{N} .

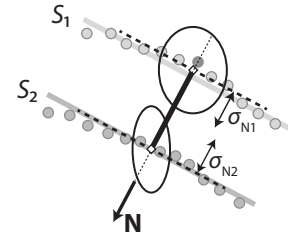


Figure 05

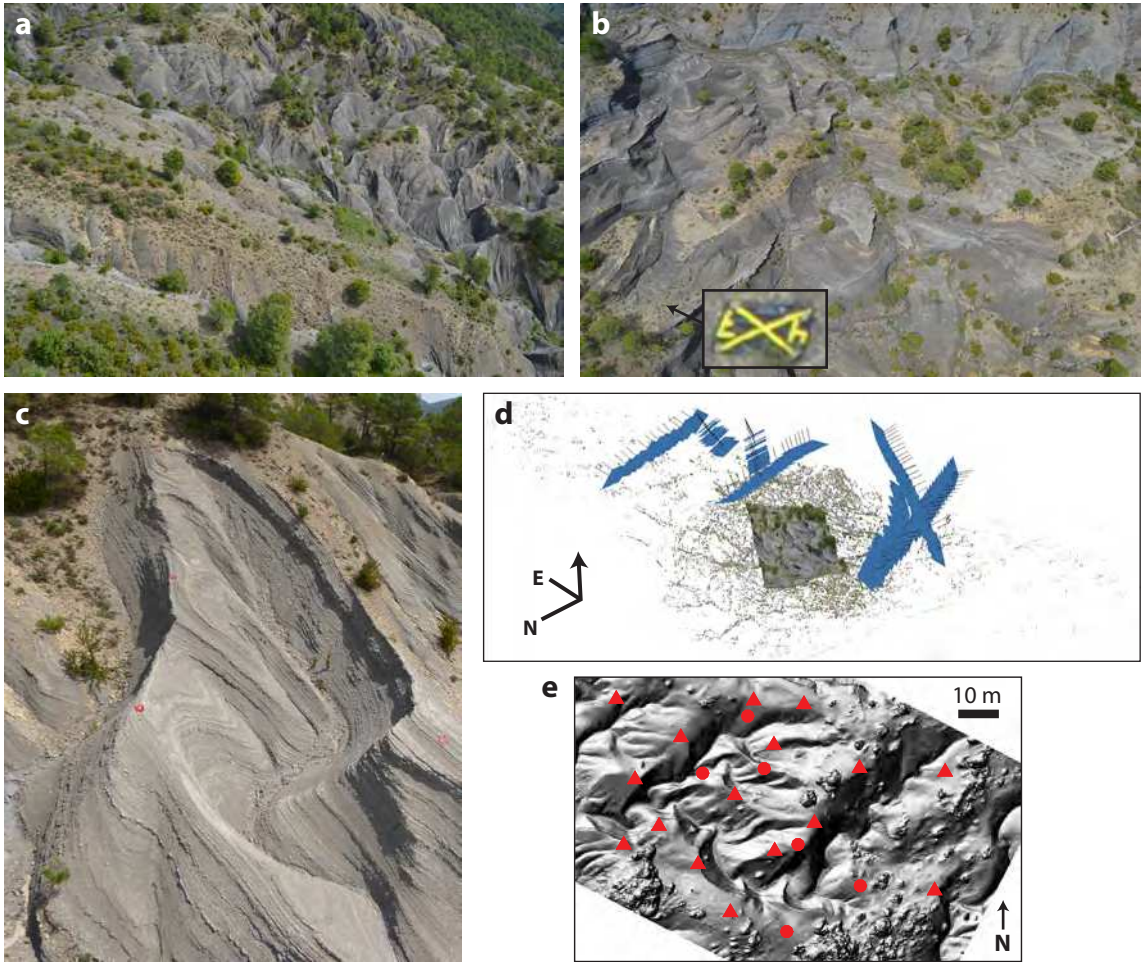


Figure 06

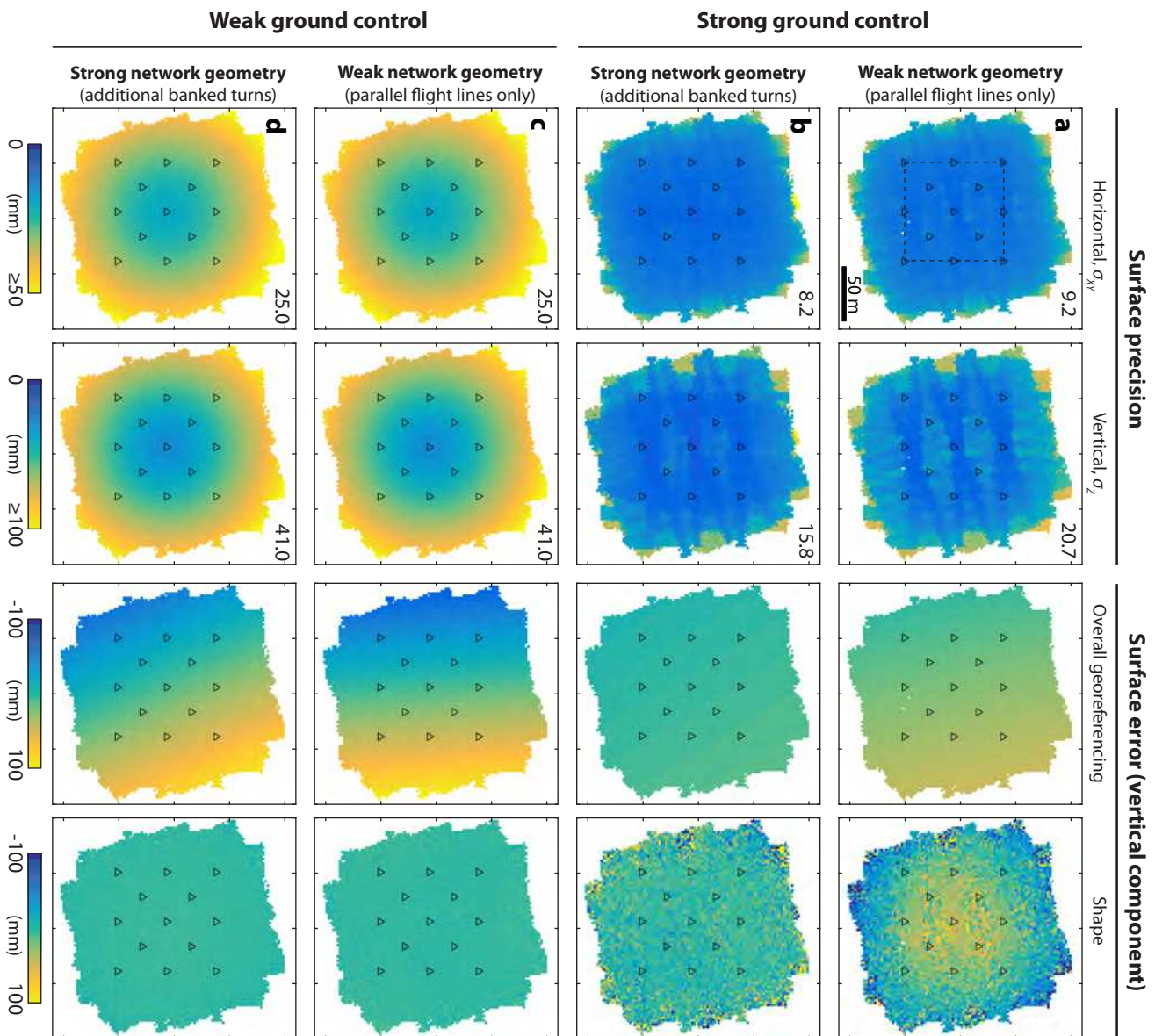


Figure 07

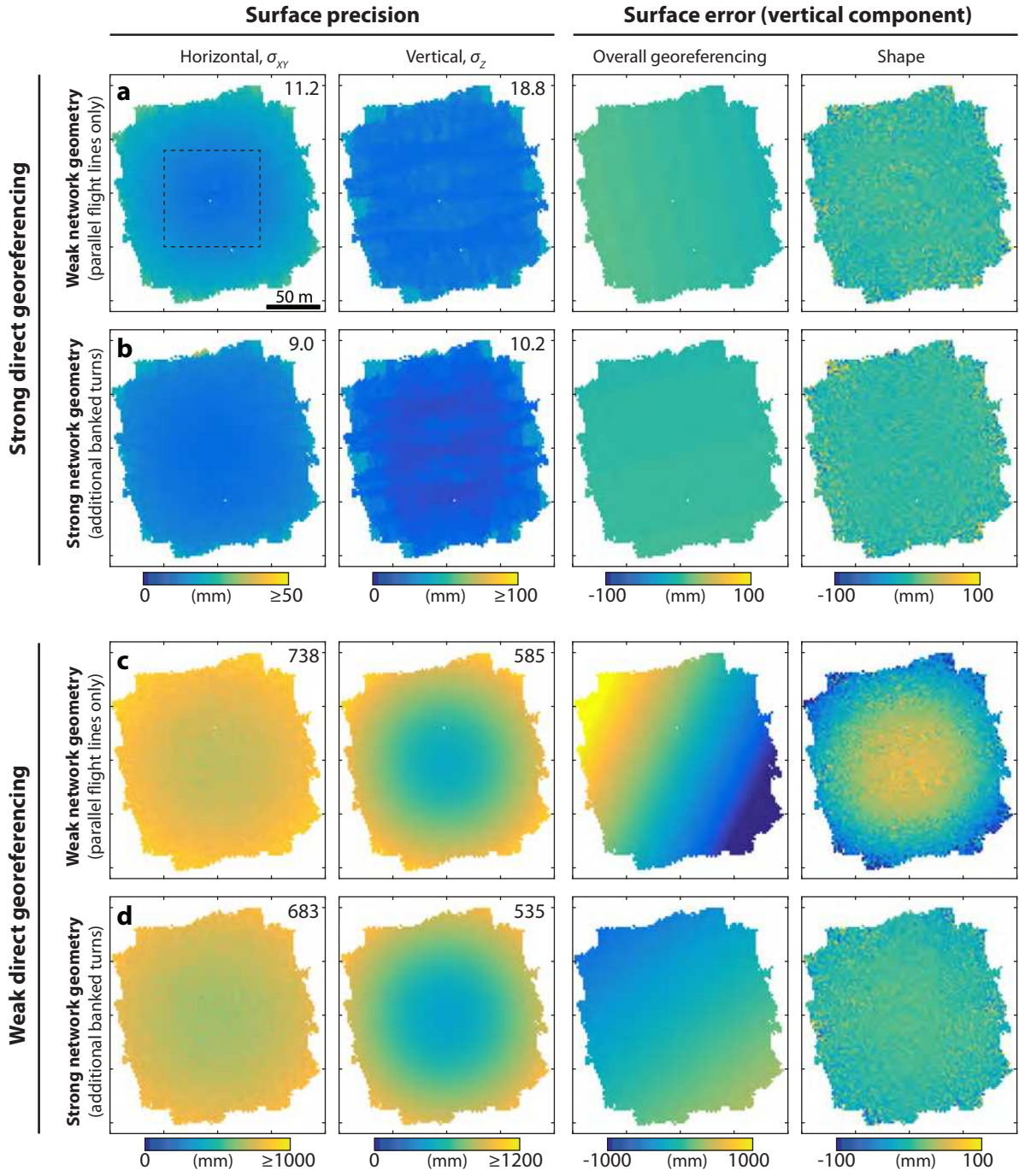


Figure 08

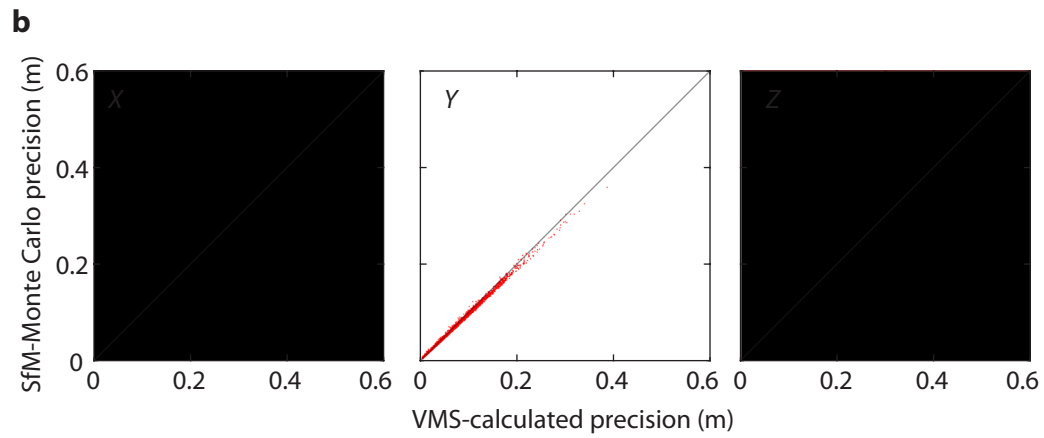
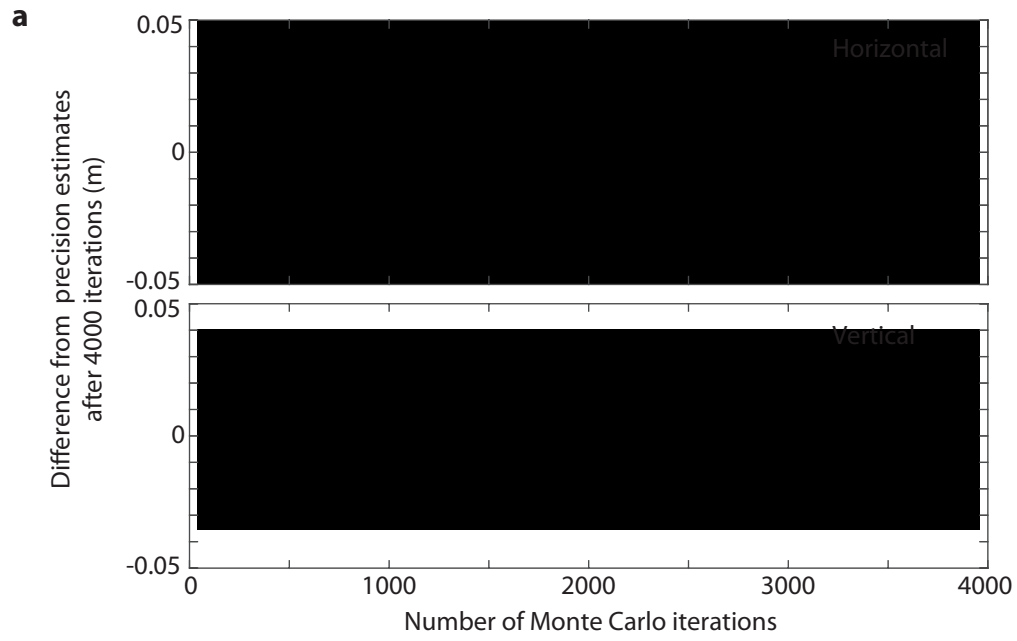


Figure 09

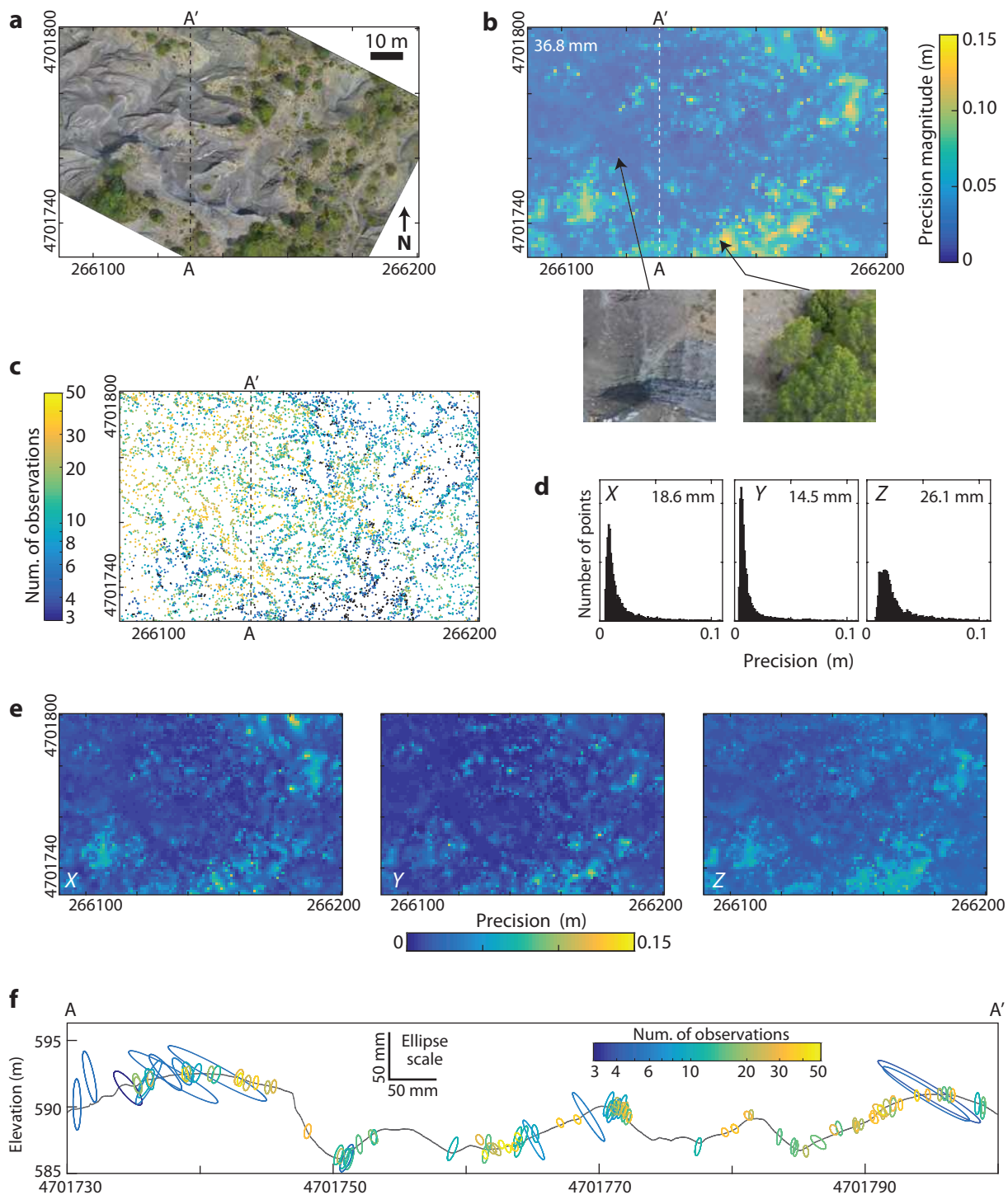


Figure 10

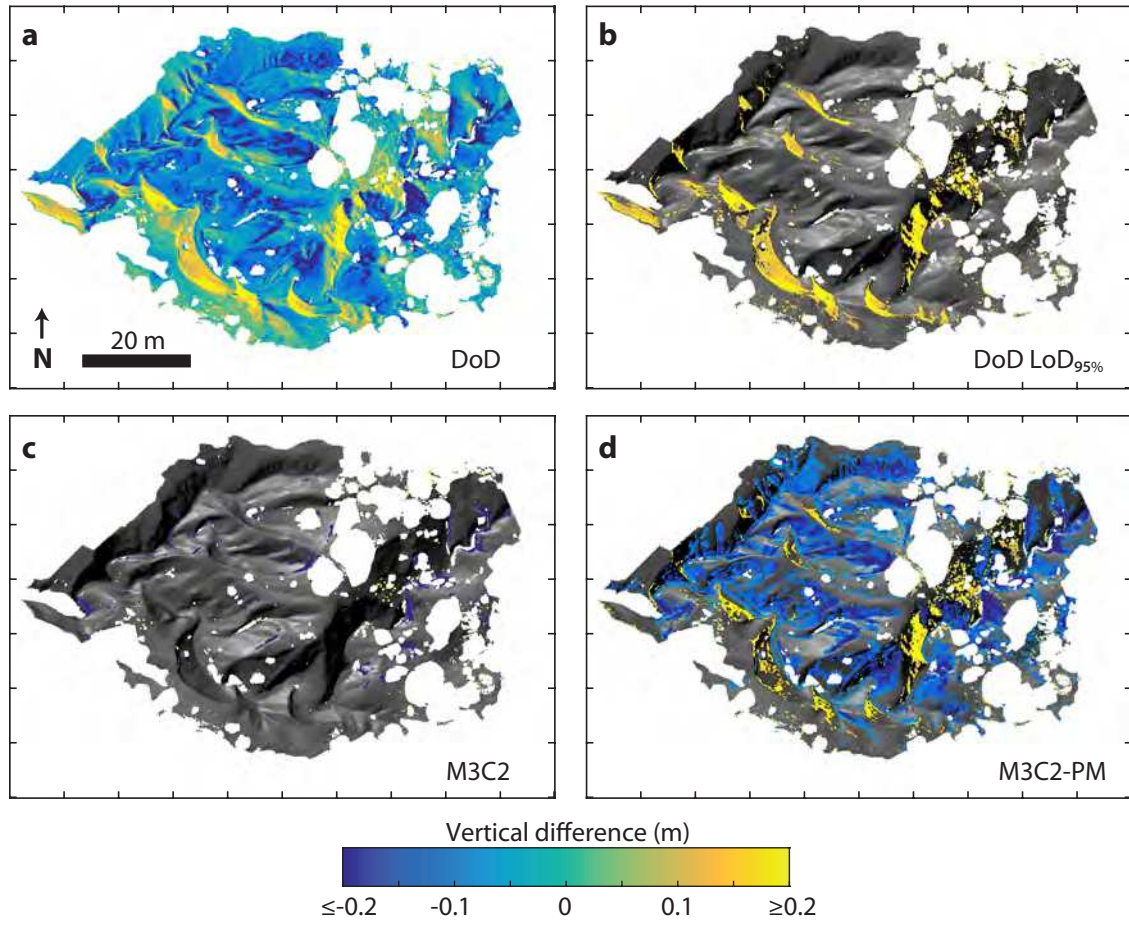


Figure 11

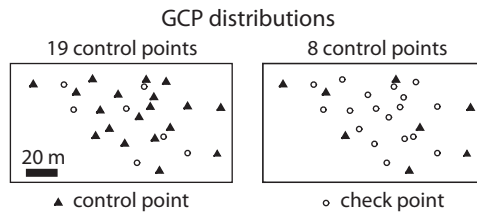
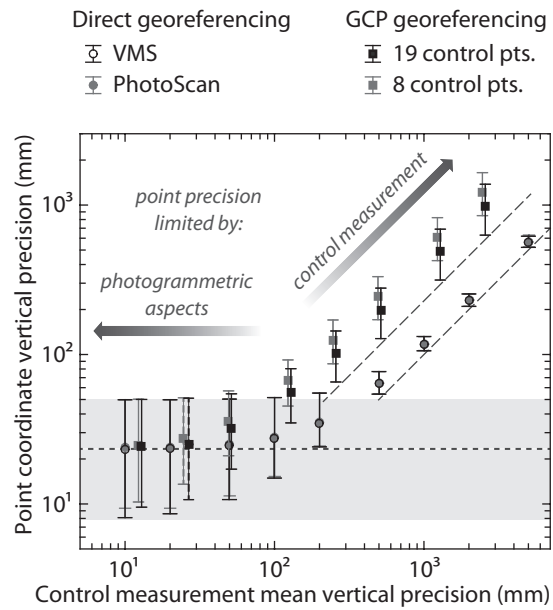


Figure 12

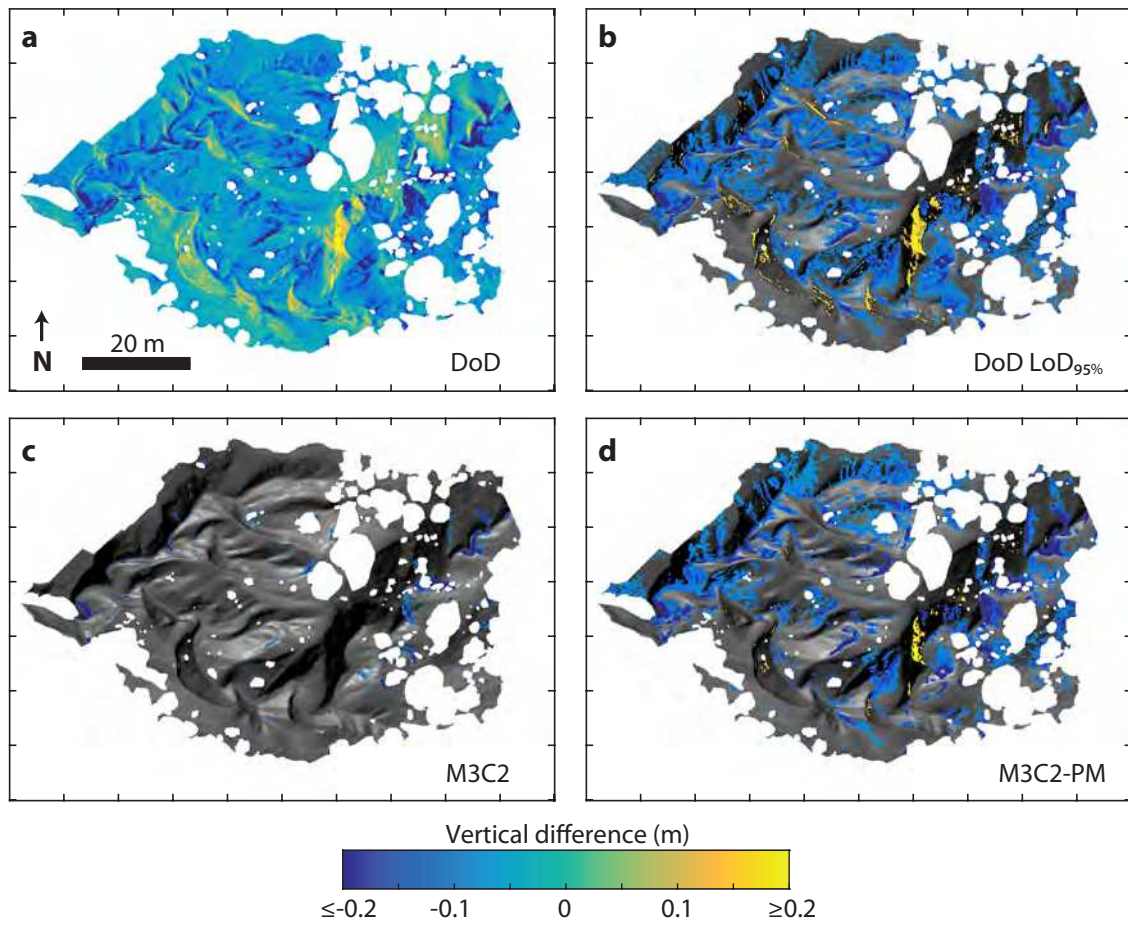


Figure 13

